

**TWO APPLICATIONS OF THE FABRY-PEROT
INTERFEROMETRIC SENSOR**

A Dissertation

by

ZHAOXIA XIE

Submitted to the Office of Graduate Studies of
Texas A&M University
in partial fulfillment of the requirements for the degree of

DOCTOR OF PHILOSOPHY

August 2006

Major Subject: Electrical Engineering

**TWO APPLICATIONS OF THE FABRY-PEROT
INTERFEROMETRIC SENSOR**

A Dissertation

by

ZHAOXIA XIE

Submitted to the Office of Graduate Studies of
Texas A&M University
in partial fulfillment of the requirements for the degree of

DOCTOR OF PHILOSOPHY

Approved by:

Co-Chairs of Committee,	Ohannes Eknoyan Henry F. Taylor
Committee Members,	Chin B. Su Gerard L. Cote
Head of Department,	Costas N. Georghiadis

August 2006

Major Subject: Electrical Engineering

ABSTRACT

Two Applications of the Fabry-Perot Interferometric Sensor. (August 2006)

Zhaoxia Xie, B.S., Shandong University, Shandong, China;

M.S., Shandong University, Shandong, China;

M.S., University of Houston

Co-Chairs of Advisory Committee: Dr. Ohannes Eknoyan
Dr. Henry F. Taylor

Two important applications of the fiber Fabry-Perot Interferometer (FFPI) sensor are investigated: (1) an optical binary switch for aerospace application, and (2) an FFPI weigh-in-motion sensor for measuring the weight of trucks traveling down a highway.

In the fiber optical switch, the FFPI sensor is bonded to a copper cantilever to sense the elongation of cavity length induced by force applied to the end of the cantilever via a pushed button. Light from a superluminescent diode light source passes through a scanned Michelson interferometer and is reflected from a sensing FFPI and a reference FFPI to produce a fringe pattern. A secondary interferometer uses a distributed feedback laser light source to compensate for irregularities in the mechanical scanning rate of the moving stage to achieve precision measurement of the optical path difference.

The system is calibrated by applying known weights to the cantilever. The elongation measured by the FFPI sensor shows excellent linearity as a function of the

force applied, and little hysteresis was observed. By comparing the measured force to a threshold, the system produces a binary signal that indicates the state of the pilot-actuated system; i. e., whether or not the button has been pushed.

In FFPI weigh-in-motion sensors system, the FFPI sensors are installed in metal bars so that they will experience the strain induced by applied loads and are connected to the Signal Conditioning Unit (SCU). The SCU determines the induced phase shift in the FFPI and produces voltage outputs proportional to the phase shifts.

Laboratory Material Testing System tests show that the fiber optic sensor response is a fairly linear function of the axial displacement. In highway tests the FFPI sensors showed strong responses and consistently reproduced the expected characteristics of truck wheel crossings. A falling weight deflectometer was used to calibrate the sensor response and predict unknown loads. All sensors in steel bars and aluminum bars showed excellent repeatability and accurate predictions, with an average relative percentage error within 2%. The study on sensor response variation with applied load positions shows a bell shaped distribution. Truck tests on the road sensors indicate that the repeatability of wheel crossings at similar position is good. The sensor can accurately measure axle spacing, speed, and truck class.

To My Late Father: Chunxi Xie

To my lovely family

ACKNOWLEDGMENTS

I would like to express my appreciation to Dr. Henry F. Taylor, for his continuous guidance and support, especially for his sincerity, generosity and patience during my research work. I would like to thank Dr. Ohannes Eknayan, co-chairman of my advisory committee, for his support and great advice during my doctoral program.

I would like to extend my appreciation to Dr. Chin B. Su and Dr. Gerard L. Cote for serving as members of my graduate committee and for providing me with suggestions and comments on my work. I would like to thank all former and current students in the solid state lab, especially Yang Ping, Dr. Pingsheng Tang, Dr. Yichao Chen for their helpful discussions.

My appreciation is also extended to John Ragsdale of the Texas Transportation Institute for his active cooperation and hard work in the weigh-in-motion project. I also thank Robert Atkins and Jim for their cooperation and help with the research. My thanks also go to Dr. Wenting Liu for providing BISAR simulation and helpful discussion, and Jerry for the saw cut in the road.

I would like to express my special appreciation to my best friend, Dr. Yuanqiu Luo, for her friendship, helpful discussions and encouragement. Special thanks to my host family, Mr. Robert Flott and Mrs. Joyce Flott, for their love and kind support.

My deepest appreciation goes to my parents, Mr. Chunxi Xie and Mrs. Yufang Li, for their love and sacrifice, especially my father, who passed away just a few years ago. He gave me the greatest encouragement in my study toward the Ph.D degree. I would

also like to express my appreciation to my brothers, sisters-in-law and nieces, and to everyone else in my family for their support.

Finally, my special thanks to my husband, Lijun Ren, who always stands by my side with support, help, patience and sacrifice.

TABLE OF CONTENTS

	Page
ABSTRACT	iii
DEDICATION	v
ACKNOWLEDGMENTS	vi
TABLE OF CONTENTS	viii
LIST OF FIGURES	xi
LIST OF TABLES	xv
 CHAPTER	
I INTRODUCTION	1
1.1 Motivation	1
1.2 Previous work	3
1.3 Objectives	5
II THEORETICAL BACKGROUND	6
2.1 Fiber interferometers	6
2.1.1 Fiber Fabry-Perot Interferometer (FFPI).....	6
2.1.2 Michelson interferometer	8
2.2 Low coherence interferometry	9
2.3 Photoelastic effect	14
III SYSTEM SETUP	17
3.1 Optical binary system overview	17
3.1.1 White light interferometer optical system.....	18
3.1.2 Calibration and test setup for binary switch.....	20
3.2 Weigh-in-motion system overview	21
3.3 Components used in the research	24
3.3.1 Light source.....	24
3.3.2 Photodetector.....	25

CHAPTER	Page
3.3.3 Translation stage and motor control system.....	26
3.3.4 The Signal Conditioning System (SCU).....	29
3.3.5 Falling Weight Deflectometer (FWD)	31
IV SIGNAL PROCESSING ALGORITHM.....	33
4.1 Summary of signal processing algorithm	33
4.2 Correction of SLD fringe data using DFB fringe data	35
4.3 Perform cross correlation of new sen[i] and ref[i]	36
4.4 Identify the central fringe in corrected correlation data	37
V OPTICAL BINARY SWITCH EXPERIMENTAL PROCEDURE AND RESULTS	40
5.1 FFPI sensor fabrication	40
5.2 Optical binary switch system overview	43
5.3 System evaluation	43
5.3.1 Signal Noise Ratio (SNR) of the system.....	43
5.3.2 Resolution test.....	44
5.3.3 Binary switch calibration, repeatability and threshold determination	46
VI FIBER OPTIC WEIGH-IN-MOTION SENSOR EXPERIMENTAL PROCEDURE AND RESULTS	50
6.1 Laboratory characterization tests and results	50
6.2 Highway tests and results	53
6.3 FFPI weigh-in-motion system installation at the Riverside Campus	55
6.4 Calibration of the FO-WIM sensor using the falling weight deflectometer	59
6.5 Evaluation of sensor performance under varying FWD load positions.....	70
6.6 Sensor performance in truck tests and analysis.....	72
VII CONCLUSIONS	80
VIII RECOMMENDATIONS	82
REFERENCES	84

Page

APPENDIX..... 88

VITA 99

LIST OF FIGURES

FIGURE	Page
1 Fiber Fabry-Perot interferometer with two internal mirrors	6
2 Free space Michelson Interferometer	9
3 Block diagram of low coherent interferometer system	12
4 WLI system for monitoring fiber interferometer	19
5 Setup for calibration of FFPI sensor	22
6 Binary fiber optic switch	22
7 FFPI weigh-in-motion measurement system	23
8 Cross section of metal bar embedded with fiber FFPI sensor	23
9 Sensors embedded in metal bars	23
10 Structure of Signal Conditioning Unit (SCU) for 24 channels	30
11 Optical system schematics of SCU	31
12 Falling weight deflectometer	32
13 Interference fringe patterns of sensing and reference sensors.....	33
14 Cross-correlation of fringe pattern before correction.....	37
15 Cross-correlation of fringe pattern after correction.....	38
16 The envelop of fringe peak of Fig. 15	38
17 FFPI sensor fabrication	41
18 Arrangement of monitoring the fabrication of FFPI	42
19 Reflected sensor signal displayed in the oscilloscope.....	42

FIGURE	Page
20 Resolution test of the optical system when the sensing sensor is free from bonding to the cantilever	46
21 Resolution test of the whole system when the sensing sensor is bonded to the cantilever	46
22 Calibration and repeatability test of the binary switch (sensor #1).....	48
23 Calibration and repeatability test of the binary switch (sensor #2).....	48
24 Steel bar response to the MTS.....	51
25 Aluminum bar response to the MTS	51
26 Dependence of the peak FFPI sensor response and axial displacement on a striking force.....	52
27 Dependence of the peak FFPI sensor response on the axial displacement.....	52
28 Locations of the sensors, in inches, along the four foot length of a metal bar.....	53
29 Response of five FFPI sensors embedded in the steel bar to a class 9 truck, as distinguished by two wheel crossings in the third group.....	54
30 Response of five FFPI sensors embedded in the aluminum bar to a class 10 truck, as distinguished by three wheel crossings in the third group.....	54
31 WIM Riverside optic sensor assembly layout.....	56
32 Sensor bar installation: Saw tooth cutting the slot in the road.....	57
33 Sensor bar installation: putting the metal bar in the slot and filling it with epoxy up to the top.....	58
34 Sensor bar installation: Final appearance after the epoxy and sealant have dried.....	58
35 One marked steel bar sensor under the center of load disk of FWD.....	60

FIGURE	Page
36 Steel bar sensor responses to the FWD load applied at ~9000 pounds	61
37 Aluminum bar sensor responses to the FWD load applied at ~7600 pounds ...	61
38 Repeatability test of the steel bar sensors.....	62
39 Repeatability test of the aluminum bar sensors.....	63
40 Sensor responses to corresponding FWD load profiles	63
41 Steel bar sensor response to different FWD applied loads.....	64
42 Aluminum bar sensor response to different FWD applied loads	65
43 Variation of steel bar sensor #3 responses with the FWD load position.....	71
44 Variation of aluminum bar sensor #12 responses with the FWD load position	71
45 BISAR simulation results of stress and strain variation with load position	72
46 Steel bar sensor responses to truck wheel crossing.....	74
47 Aluminum bar sensor responses to truck wheel crossing	74
48 Repeatability: two steel bar sensor responses to truck wheel crossings at same position	76
49 Repeatability: two aluminum bar sensor responses to truck wheel crossing at same position.....	77
50 Steel bar sensor #3 output amplitude variation with FWD load positions.....	78
51 Aluminum bar sensor #13 output amplitude variation with FWD load positions.....	78
52 Suggested sensor distribution across a lane	83

LIST OF TABLES

TABLE	Page
1	Optical and electrical characteristics of SLD 24
2	Optical and electrical characteristics of DFB laser 26
3	3a Absolute maximum rating of the photodetector 27
4	3b The optical and electrical characteristic of the photodetector..... 27
5	Measured sensor number and position to the marked end of metal bar 60
6	Linearity coefficients of steel bar sensors 65
7	Linearity coefficients of aluminum bar sensors 65
8	Prediction and RPE's of the steel bar FWD applied loads of data V series..... 67
9	Prediction and RPE's of the steel bar FWD applied loads of data X series..... 68
10	Prediction and RPE's of the aluminum bar FWD applied loads..... 69
11	Parameters of the truck..... 73

CHAPTER I

INTRODUCTION

1.1 Motivation

The first objective of this research is to develop an optical binary switch to be used in aircraft. Present aircraft utilize electrical wiring for transmitting sensor signals in systems for controlling elevators, rudders, and other flight-critical elements. There is strong interest in the avionics community in increasing the safety and reliability of aircraft while reducing operating and maintenance costs by replacing conventional wire systems with fiber optics. Extensive research is performed on structure health monitoring (SHM) of aerospace vehicles and aircraft [1]. Fiber optical sensors have remarkable advantage in meeting the minimal size and weight requirement due to improved multiplexing capability. Other major benefits include low cost and immunity to electromagnetic interference (EMI) and lightning. One important type of sensor is a binary switch which is actuated when the pilot presses a button. The signal from the switch is a “0” when no force is applied and a “1” when the operator-induced strain in the sensing element exceeds a threshold [2].

The journal model is *IEEE Journal of Lightwave Technology*.

Weigh-in-motion systems are devices that are capable of weighing vehicles in-motion at speeds up to and including typical mainline highway speeds. In order to ensure public safety and highway infrastructure longevity, most commercial carriers (big trucks) on the highway must be weighed everyday. Due to the sheer volume of car and truck traffic on our highways, current weighing systems using slow and cumbersome static scales aren't a viable option. Furthermore there is a growing concern over the increase in overweight truck loads on highways caused by economic growth. Pavement performance is influenced greatly by truck traffic loading rather than traffic repetition, Therefore there's a strong demand for an economic and effective WIM system.

The second objective of this research is to investigate the feasibility of a weigh-in-motion (WIM) measurement system utilizing fiber Fabry-Perot optical sensors. This is the first investigation of this unique sensor as an alternative to piezoelectric sensors for the WIM applications. Disadvantages of present day piezoelectric-based WIM systems include: maintenance difficulties, susceptibility to corrosion, occurrence of erroneous readings and damage due to power surges, signal crosstalk from adjacent traffic lanes, and high cost. The fiber optic Fabry-Perot sensor is more durable, immune from electromagnetic interference and crosstalk, electrically isolated from the monitoring equipment, free from corrosion effects, suitable for remote monitoring with multi-km separation between the signal conditioning unit (SCU) and the sensors, and potentially cost-effective when many sensors are operated from a single SCU[3-7].

1.2 Previous Work

Fiber optics is playing an increasing role in data transmission, signal distribution, and sensing. Extensive research has been performed in using communication-based optical fibers for sensing physical parameters such as temperature, pressure, strain, displacement and refractive index etc., due to many of their many attractive features that supersede the conventional sensor. Application of fiber optic sensors can be found in areas such as aerospace, civil construction, the transportation industry, biology, medicine, and manufacturing.

Optical fiber sensors can be classified as extrinsic sensors and intrinsic sensors. For the extrinsic sensors the fiber conducts light to and from the measurand outside the fiber while for the intrinsic sensor the fiber itself senses the perturbation to be investigated. By different modulations of light in response to the measurand, these sensors can also be classified as intensity sensors (amplitude modulated), phase modulated interferometer sensors and polarization modulated sensors. Among them, the interferometer sensor can provide the highest sensitivity for measuring physical changes.

There are two schemes in interferometric sensors aimed at determining the optical path difference (OPD): (1) high coherence interferometric sensors using laser sources have the advantage of high speed dynamic measurement but usually cannot provide absolute OPD result; (2) low coherent interferometry (LCI) also called white light interferometry (WLI) uses low coherent light sources such as a light emitting diode or superluminescent diodes (SLD). WLIs, in principle, have the advantage of achieving absolute OPD measurement from “cold start” with Michelson, Mach-Zehnder, Fabry-

Perot or other configuration. They can be used in static or quasi-static parameters measurement such as temperature, pressure etc.

The first intrinsic Fabry-Perot interferometer (FFPI) sensors were fabricated by C. E. Lee and Henry F Taylor at Texas A&M University in 1988 [8] . The FFPI have unique advantages over other fiber-optic sensing elements, as well as exhibit high sensitivity and rapid response. Intensive research was conducted on pressure and temperature sensor systems devoted to developing a practical measurement system by using FFPI's [2, 8-20].

Considerable research into sensor systems of dynamic pressure or strain have been carried out at Texas A&M University in order to measure current [18], engine pressure [19, 20] and railroad bridge monitoring systems [21]. The fundamental methodology is to utilize the phase shift undergone by the reflected light from FFPI sensors due to various environmental perturbations. The interference fringe data is processed by the signal conditioning unit (SCU) with a microprocessor to determine the phase shift in the fiber interferometer, and to produce voltage outputs proportional to the phase shifts.

For measuring the absolute OPD of static or quasi-static parameters from the cold start, i.e. without input the initial value of the parameter whenever the system is turned on, low-coherent interferometry has drawn more and more attention from researchers[22-29]. Study into LCI's using dual FFPIs was also performed at TAMU [12-15, 22]. Compared to laser sources, this type has the advantage of identifying the interference fringe order with a high level of precision from the output pattern of the

interferometer using a broadband source; compared to some reported extrinsic Fabry-Perot temperature sensors also based on low coherence interferometry [24-26], it has the advantage of high resolution and a large dynamic range.

1.3 Objectives

The primary objectives of this research are:

1. To develop an optical binary switch system which is actuated by the pilot pressing a button based on low coherence interferometry. The signal from the switch is a “0” when no force is applied or a “1” when the operator-induced strain in the sensing element exceeds a threshold.

2. To investigate the feasibility of a weigh-in-motion (WIM) measurement system utilizing fiber Fabry-Perot optical sensors.

CHAPTER II

THEORETICAL BACKGROUND

2.1 Fiber Interferometers

The four most commonly used types of classical fiber interferometers are Michelson, Mach-Zehnder, Sagnac and Fabry-Perot interferometers. The basic working principle of an interferometer is that it divides a beam into either two or many beams, the beams travel through different optical paths. Thus when reunited the light wave amplitudes add coherently, and interfere with each other. In this research we mainly use Michelson and Fabry-Perot interferometers.

2.1.1 Fiber Fabry-Perot Interferometer (FFPI)

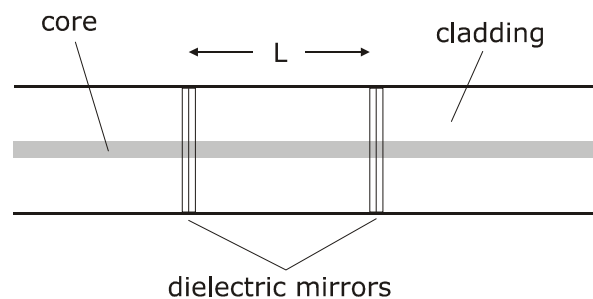


Fig. 1. Fiber Fabry-Perot interferometer with two internal mirrors

The Fabry-Perot interferometer is a typical multiple beam device. The output depends upon the successive multiple reflections of an input beam between the two

mirrors forming the etalon. It serves as a basic type of laser resonant cavity and as a filter in communication systems. It is widely used in laser and optics research.

The fiber Fabry-Perot interferometer is composed of two dielectric internal mirrors that form a Fabry-Perot cavity within a single mode fiber, as shown in Fig. 1. The sensor is generally monitored in reflection, and the magnitude of the optical signal P_r is determined by the interference of light reflected by the two mirrors

$$P_r = P_i * (R_1 + R_2 - 2\sqrt{R_1 * R_2} * \cos \varphi). \quad (2.1)$$

where P_i and P_r are the incident and reflected optical powers, R_1 and R_2 are the mirror reflectances (R_1 and R_2) $\ll 1$, L is the cavity length (mirror separation), and φ is the round-trip phase shift of the light inside the cavity.

If the reflectances R_1 and R_2 are the same, with $R=R_1=R_2$, equation (2.1) becomes

$$P_r = 2RP_i(1 - \cos \varphi) . \quad (2.2)$$

The round trip phase shift can be expressed as

$$\varphi = \frac{4\pi n \nu L}{c} = \frac{4\pi n L}{\lambda} \quad (2.3)$$

where n is the refractive index, ν is the optical frequency, L is the cavity length of FFPI, and c is the free space wavelength of the light source.

The reflective power P_r will change in response to the variation of phase φ . φ can be expressed as

$$\varphi = \varphi_0 + \Delta\varphi_L + \Delta\varphi_\nu + \Delta\varphi_T \quad (2.4)$$

with

$$\Delta\varphi_L = \frac{4\pi}{\lambda}(n\Delta L + L\Delta n) \quad (2.5)$$

$$\Delta\varphi_\nu = \frac{4\pi L}{c}\left(n + \nu \frac{dn}{d\nu}\right) \quad (2.6)$$

$$\Delta\varphi_T = \frac{4\pi}{\lambda}\left(L \frac{d\nu}{dT} + n \frac{dL}{dT}\right) \quad (2.7)$$

where φ_0 is the initial round phase shift, and ΔL , $\Delta\nu$ and ΔT are the changes in length, frequency and temperature, respectively.

The FFPI can sense any physical perturbation, including perturbations in temperature, pressure and strain that can change the optical path nL . The reflected optical power is the coherence summation of the two waves reflected from the two mirrors and is converted to electrical signal by a photodetector. Increasing the cavity length L will increase the sensitivity of the sensor system.

2.1.2 Michelson interferometer

The Michelson interferometer is widely used in the optical industry for testing lenses and prisms, measuring the refractive index, or examining minute details of the surface. The Michelson interferometer is shown in Fig. 2.

Light from the source is divided by the beam splitter into two paths. As the light is reflected from the mirrors ends, the beam passes back into the beamsplitter towards the photodetector where the phase shift between the two beams is detected. The difference of phase shift can be represented as

$$\Delta\Phi = \frac{4\pi n(L_1 - L_2)}{\lambda} \quad (2.8)$$

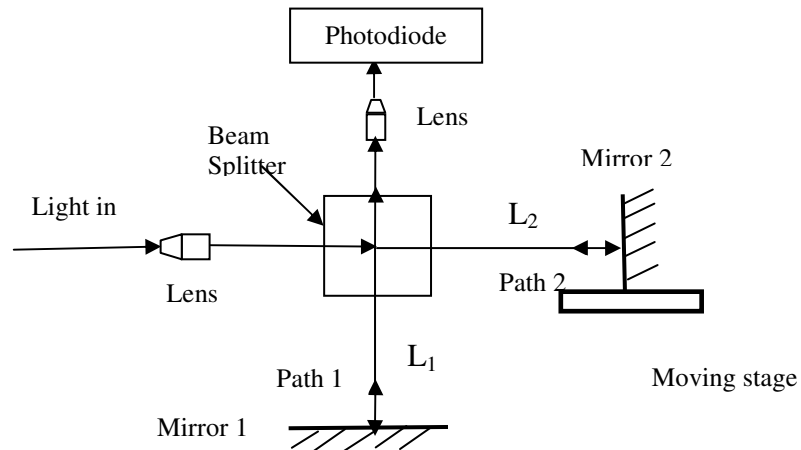


Fig. 2 Free space Michelson interferometer

where n is the refractive index of the fiber used, L_1 and L_2 are the lengths of the two paths, and λ is the central wavelength of the light source. Usually a moving stage is used to obtain the interference fringe pattern.

The detected light intensity is

$$I = I_1 + I_2 + 2\sqrt{I_1 I_2} \cos(\Delta\Phi) \quad (2.9)$$

2.2 Low Coherence Interferometry

Low coherence interferometry (LCI) is designed to measure the optical path difference of the sensing interferometer by using a broadband light source (coherence length $\sim 20\text{-}50 \mu\text{m}$).

Equation (2.9) is valid only if the light source is coherent, i.e. the light source is monochromatic. For the incoherent source there's no interference, so $I=I_1+I_2$; for the broad band light source, $\Delta\lambda=10\sim 100\text{nm}$, the reflected power for each wavelength is:

$$I_{r1} = 2I(v_1)(1 - \cos(2\pi\Delta L v_1 / c))$$

$$I_{r2} = 2I(v_2)(1 - \cos(2\pi\Delta L v_2 / c))$$

.....

$$I_m = 2I(v_n)(1 - \cos(2\pi\Delta L v_n / c)) \quad (2.10)$$

so the total intensity is
$$I_t = 2 \sum_{i=1}^n [I(v_i)(1 - \cos(2\pi\Delta L v_i / c))] . \quad (2.11)$$

Here the $\Delta L = 2(L_1 - L_2)$ is the optical path difference. The interference term is

$$I(v_1, v_2, \dots, v_n) = 2 \sum_{i=1}^n I(v_i) \cos(2\pi\Delta L v_i / c) . \quad (2.12)$$

For light of a continuum spectrum, the intensity is given by the spectral density of $S(v)$, the interference term is

$$I(v_1, v_2, \dots, v_n) = 2 \int_0^{\infty} S(v) \cos(2\pi\Delta L v / c) dv . \quad (2.13)$$

Assuming that the spectral distribution of the source is a Gaussian spectrum, which is a reasonably good approximation for many SLD's, the spectral power density of the light incident upon the sensor FFPI can be written as

$$S(v) \propto e^{-\frac{(v-v_0)^2}{\Delta v}} \propto A_0 e^{-\rho^2(v-v_0)^2} . \quad (2.14)$$

Here, $\rho = \pi L_c / 2c$, A_0 is constant, c is the speed of light in the free space, and L_c is the coherence length of the light source

$$L_c = c \tau_c = k \frac{c}{\Delta v} = k \frac{\lambda^2}{\Delta \lambda} \quad (2.15)$$

where τ_c is the coherence time, λ is the center wavelength of the source, and $\Delta\nu$ and $\Delta\lambda$ are spectral width of the source in frequency and in wavelength, respectively. According to the spectral line shape, k is determined as follows [28]

$$\text{Gaussian line: } k = \sqrt{\frac{2 \ln 2}{\pi}} = 0.664$$

$$\text{Lorentzian line: } k = \frac{1}{\pi} = 0.318$$

$$\text{Rectangular line: } k = 1.$$

Then the fringe signal

$$\begin{aligned} I(v_1, v_2, \dots, v_n) &= 2 \int_0^{\infty} S(v) \cos(2\pi\Delta L v / c) dv \\ &\propto A_0 e^{-\left(\frac{2\Delta L}{L_c}\right)^2} \cos(2\pi\Delta L / \lambda) \end{aligned} \quad (2.16)$$

with $\lambda=c/v_0$. An interferometer pattern is observed when the moving stage scan so that $2|L_1-L_2|<L_c$. The maximum amplitude of the fringe pattern is observed when $L_1=L_2$. As the optical path difference ΔL increases, the decrease in fringe visibility is given by

$$V = 0.5 \exp\left[-\left(\frac{2\Delta L}{L_c}\right)^2\right] \quad (2.17)$$

The basic setup of the LCI is shown in Fig. 3. Light from a broadband light source is coupled into a processing interferometer, such as a scanned Michelson interferometer, and then into the sensing interferometer. In our system we use an FFPI sensor, which assumes that the reflectance of the two mirrors in the FFPI mirrors is $\ll 1$ (low-finesse interferometer). The round trip phase shift in the sensing interferometer

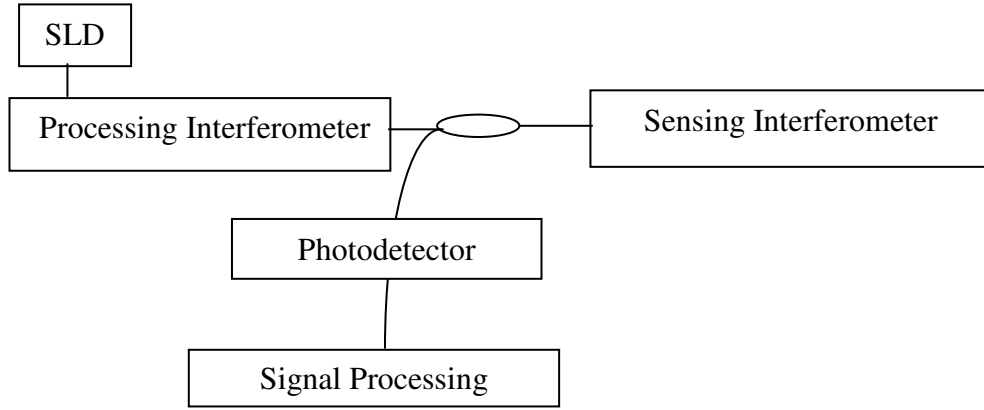


Fig. 3. Block diagram of low coherent interferometer system

φ_s can be written as

$$\varphi_s = \frac{2\pi\nu L_s}{c} \quad (2.18)$$

where L_s is the optical path difference in the sensing interferometer, $L_s=2nL$, and n is the effective refractive index of the fiber mode.

The phase difference in the processing interferometer φ_p is:

$$\varphi_p = \frac{2\pi\nu L_p}{c} \quad (2.19)$$

where L_p is the optical path difference for the two arms of the processing interferometer.

The spectral power density of the light transmitted by the processing interferometer dP_p/d

ν can be written as

$$\frac{dP_p}{d\nu} = \frac{dP_{SLD}}{d\nu} \frac{(1 + \cos \varphi_p)}{2} \quad (2.20)$$

The total power incident on the processing interferometer P_{SLD} is given by integrating the spectral power density over the spectrum of the light source

$$P_{SLD} = \int \frac{dP_{SLD}}{d\nu} d\nu \quad (2.21)$$

The reflected power from the sensing interferometer P_r can be written as

$$\frac{dP_r}{d\nu} = 4R\alpha \frac{dP_{SLD}}{d\nu} \frac{(1 + \cos \varphi_p)}{2} \quad (2.22)$$

where R is the reflectance of the mirrors in the sensing interferometer, with $R \ll 1$, α is a constant that represents the optical loss between the sensor and reference interferometers.

If we combine equations (2.21) and (2.22), we get:

$$\frac{dP_r}{d\nu} = 4R\alpha \frac{dP_{SLD}}{d\nu} (1 + \cos \varphi_p)(1 + \cos \varphi_s) \quad (2.23)$$

In computing the output power we need to integrate equation 2.23 with respect to the frequency over the spectrum of the light source. Assuming that the spectrum is sufficiently broad so that the integral extends over many periods of the cosine function, we get

$$\int \cos \varphi_p d\nu = \int \cos \varphi_s d\nu = 0 \quad (2.24)$$

As stated above, the spectral power density of SLD can be written as in equation 2.14, then

$$\frac{dP_{SLD}}{d\nu} = R e^{-\rho^2(\nu-u_0)^2} \quad (2.25)$$

Substituting equations 2.24 and 2.25 into 2.23, then integrating yield the result

$$P_R = R\alpha P_{SLD} \left\{ 1 + 0.5 \cos \frac{2\pi\Delta L_{OPD}}{\lambda} \right\} \exp \left[- \left(\frac{2\Delta L_{OPD}}{L_c} \right) \right] \quad (2.26)$$

with ΔL_{OPD} the path difference of the two interferometers, $\Delta L_{OPD} = |L_s - L_p|$.

2.3 Photoelastic Effect

The photoelastic effect describes the relationship between the material strain and the resulting refractive index change in the material. When a homogeneous continuum optical medium is subjected to external forces, changes in the refractive index are induced. In standard contracted notation, the effect is described by

$$\Delta \left(\frac{1}{n^2} \right)_i = \sum_j P_{ij} S_j \quad (i, j=1 \text{ to } 6) \quad (2.27)$$

where $\Delta \left(\frac{1}{n^2} \right)$ denotes the change of indicatrix, P_{ij} refers to the coefficient of the strain-optic tensor, $S_1, S_2,$ and S_3 are the principle strains, and S_4, S_5 and S_6 are the sheer strains. For fused silica, the photo elastic effect is small, and $\Delta(1/n^2)_i = -2\Delta n_i/n^3$ can be assumed. For linear stress-strain, S_j can be expressed as

$$S_j = \begin{bmatrix} -\gamma \epsilon_0 \\ -\gamma \epsilon_0 \\ \epsilon_0 \end{bmatrix} \quad (2.28)$$

Here ϵ_0 is the strain in z direction; γ is the Poisson's ratio which is determined by material property.

The strain-optic tensor for fused silica is

$$\begin{bmatrix} P_{11} & P_{12} & P_{12} & 0 & 0 & 0 \\ P_{12} & P_{11} & P_{12} & 0 & 0 & 0 \\ P_{12} & P_{12} & P_{11} & 0 & 0 & 0 \\ 0 & 0 & 0 & P_{44} & 0 & 0 \\ 0 & 0 & 0 & 0 & P_{44} & 0 \\ 0 & 0 & 0 & 0 & 0 & P_{44} \end{bmatrix} \quad (2.29)$$

where P_{11} and P_{12} are the individual strain-optic coefficients, and $P_{44}=(P_{11}-P_{12})/2$.

Light propagating through a longitudinally strained single mode fiber is polarized along the transverse direction ($i=1, 2$), and therefore we can see a change in the refractive index

$$\Delta n_x = -\frac{n^3}{2} \sum_j P_{1j} S_j = -\frac{n^3}{2} [S_1(P_{11} + P_{12}) + P_{12}S_3]$$

$$\Delta n_y = -\frac{n^3}{2} \sum_j P_{2j} S_j = -\frac{n^3}{2} [S_1(P_{11} + P_{12}) + P_{12}S_3]$$

$$\text{thus } \Delta n_x = \Delta n_y = -\frac{n^3}{2} [(P_{11} + P_{12})S_1 + P_{12}S_3] \quad . \quad (2.30)$$

To the FFPI sensor, when used as a strain sensor with temperature and pressure held constant, the round trip phase shift of the FFPI sensing element ϕ in response to an axial strain ε is given by combining equations 2.5 and 2.30. As a result we get

$$\Delta\phi = \frac{4\pi n L \varepsilon}{\lambda} \{1 - 0.5n^2 [P_{12} - \gamma(P_{11} + P_{12})]\} \quad (2.31)$$

For a fused-silica fiber, with $n=1.45$, $P_{11}=0.12$, $P_{12}=0.27$, and $\gamma=0.17$, we find that

$$\varepsilon = \frac{\lambda \Delta\phi}{14.3L} \quad . \quad (2.32)$$

Another case to consider is one in which a uniform radial pressure P is applied to the fiber, which causes a refractive index change. In that case, $\epsilon=P/E$, where P is the pressure applied, and E is the Young's modulus of the material. The change in the fiber refractive index for light polarized perpendicular to the fiber axis (due to the longitudinal stress) is given by

$$\frac{\Delta n_x}{n} = \left(\frac{n^2 P}{2E} \right) (P_{12}(1-\nu) - \nu P_{11}) \quad . \quad (2.33)$$

The change in optical path length of the interferometer owing to the strain can be expressed as

$$\frac{\Delta(n_x L)}{nL} = \frac{\Delta n_x}{n} + \frac{\Delta L}{L} \quad . \quad (2.34)$$

The round-trip phase shift

$$\Delta \varphi = \frac{4\pi \Delta(nL)}{\lambda} \quad (2.35)$$

for a fused silica fiber $E = 7 \times 10^{10} \text{ N/m}^2$, from equation (2.33), (2.34), and (2.35) we can get

$$P = \frac{\lambda \Delta \varphi}{8.86 \times 10^{-11} L} \quad (2.36)$$

with N/m^2 as the unit for P .

CHAPTER III

SYSTEM SETUP

3.1 Optical Binary System Overview

In the optical switch applications, it is necessary to determine the state of the switch (i. e., whether or not a force is applied) from a “cold start”. This means that if the power of the monitoring system is turned on with no prior knowledge of the history of the system, it is necessary to determine whether or not a force is being applied. This implies that the system must be capable of a static measurement of the length of the FFPI.

The requirement of static measurement capability rules out the use of a simple laser monitoring system, which is not capable of strain measurement from a “cold start”. The alternative is a “white light interferometer” (WLI) shown in Fig. 4. The WLI achieves the static measurement capability by using a broadband light source instead of a narrowband laser. Presently we use a 1325nm superluminescent diode (SLD) as the broadband light source.

The FFPI sensor is bonded to a copper cantilever. A force applied to an end of the cantilever causes it to bend, resulting in an elongation of the FFPI sensor. Light from the SLD passes through the Michelson interferometer and is reflected from a sensing FFPI and a reference FFPI, producing a fringe pattern. The temporal displacement of the two central fringes is proportional to the change in the OPD of the sensing FFPI. A secondary interferometer uses a distributed feedback (DFB) laser light source to compensate for irregularities in the mechanical scanning rate of the moving

stage. High resolution can be achieved by using a cross-correlation algorithm data processing using C++.

3.1.1 White light interferometer optical system

The monitoring setup shown in Fig. 4 consists of two bulk scanned Michelson interferometers sharing a common mirror mounted translation stage [29]. The interferometer using the SLD light source monitors the FFPI; while a second interferometer uses a distributed feedback (DFB) laser.

All fiber interferometers have the advantage of light weight and small size, are less susceptible to vibrations, and alignment problems are totally eliminated by using all-fiber components. However, fiber interferometers have the disadvantage that the state of polarization (SOP) of the light changes randomly. Its SOP is very sensitive to external perturbations such as temperature and strain. Polarization changes in the arms of the interferometer will cause fluctuations in the fringe visibility.

The bulk free space Michelson interferometer is not only immune to random changes in the SOP in fiber propagation paths; it also avoids difficulties in fabricating length-matched arms for all-fiber Fabry-Perot or Mach-Zehnder interferometers. It also has the advantage of providing large dynamic range so that it can be used for the coherent multiplexing of many sensors.

However, it's difficult to achieve an extremely high resolution in the OPD measurement with a mechanically scanned interferometer, due to the random variations in the motor rate of the motor-driven translation stage. This is overcome by using a

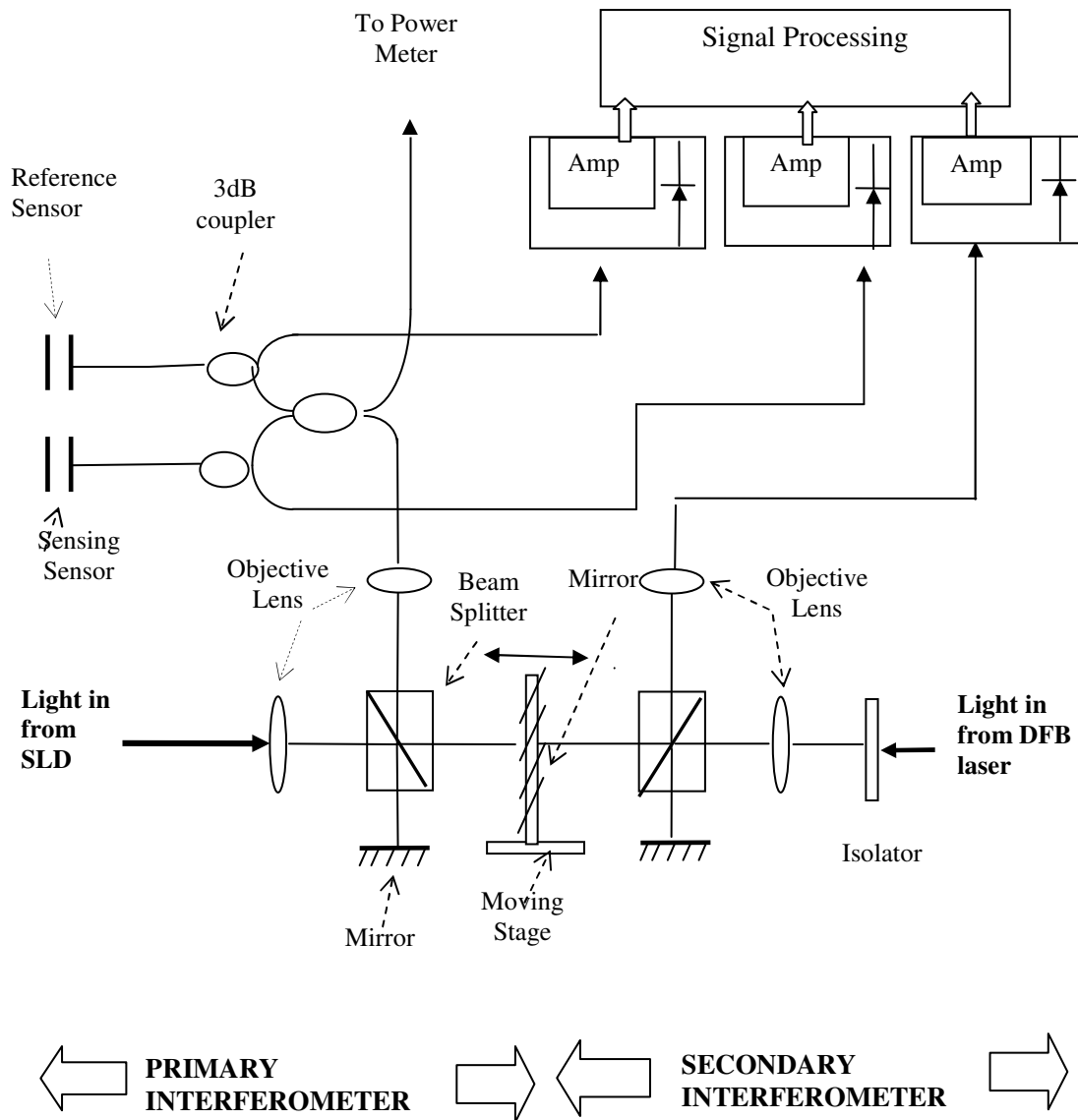


Fig. 4. WLI system for monitoring fiber interferometer

second Michelson interferometer with a distributed feedback (DFB) laser to accurately monitor the displacement of the scanning mirror in the SLD interferometer accurately.

The same mirrors in the mounted translation stage ensure the same displacement in the two interferometers. The output signal from the DFB interferometer can be assumed to be a perfect sine function. The periodicity of the DFB fringe pattern is used to determine the exact position of the stage and to compensate for the irregularity of mechanical stage motion.

3.1.2 Calibration and test setup for binary switch

The arrangement for calibration of the fiber-optic switch is shown in Fig. 5. The FFPI sensing element is bonded to a copper cantilever. A force applied to the end of the cantilever causes it to bend, resulting in an elongation of the FFPI. The response of the switch to an applied force is tested by applying known weights to the cantilever.

When a force is applied to the cantilever, according to classical elasticity theory, $M/I = \sigma/(h/2)$. Here M is the bending moment, σ is the stress, h and b are the thickness and width of the beam, respectively, and $I=bh^3/12$ is the second moment of area of the beam. The bending moment is $M=G(L_b-L_f)$. Here G is the weight applied to the beam, L_b is the length of the beam, and L_f is the distance of one point in the FFPI cavity to the fixed end of the beam. The stress can be expressed as $\sigma=\varepsilon E$. From the above discussion, we can get:

$$\varepsilon = 6(L_b - L_f)G/(Ebh^2) \quad (3.1)$$

Averaging the strain in the cavity of length L gives:

$$\varepsilon = 6(L_b - L/2)G/(Ebh^2) \quad (3.2)$$

This equation shows that when the FFPI cavity is bonded at the fixing end, as indicated in Fig. 5, we can get the maximum level of strain.

A switch configuration employing an FFPI element bonded to a cantilever is shown in Fig. 6. The design ensures that no mechanical contact with the cantilever occurs until the button is pushed. The two legs move with the pushbutton. The shorter one exerts the force to the cantilever and causes an elongation of FFPI cavity; the longer leg ensures that the cantilever will not be over-bended.

3.2 Weigh-in-motion System Overview

The whole system consists of a fiber-embedded metal bar which senses the pressure induced when the truck wheels pass, a signal conditioning unit (SCU) to provide laser light source, signal processing and output signal, and a data acquisition system and computer, as shown in Fig. 7.

Sensors were embedded in both steel and aluminum bars. The lengths of the bars were 1 foot for lab calibration and 4 or 5 feet for road tests. The sensor was bonded with polyimide in a 1/4×1/8 inch groove in the metal bar (Fig. 8) with cross-sectional dimensions of 1×1 inch. The groove was then filled with high temperature red silicone.

In lab tests we embedded one sensor in the metal bar. In road tests 5 sensors were embedded in each bar, as shown in Fig. 9. The distribution of sensors was intended to ensure that the right side of the tires of the truck will pass close to one or more of the sensors.

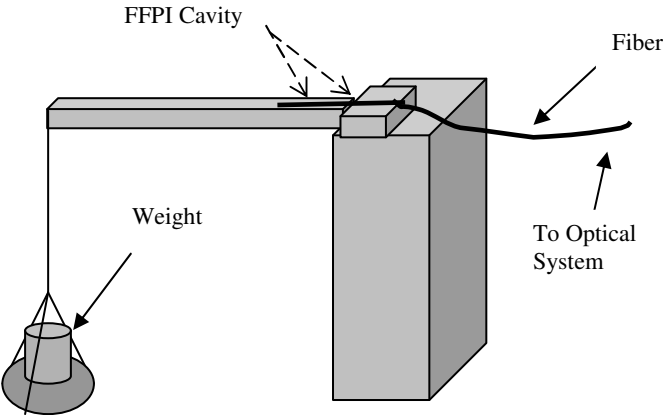


Fig. 5. Setup for calibration of FFPI sensor

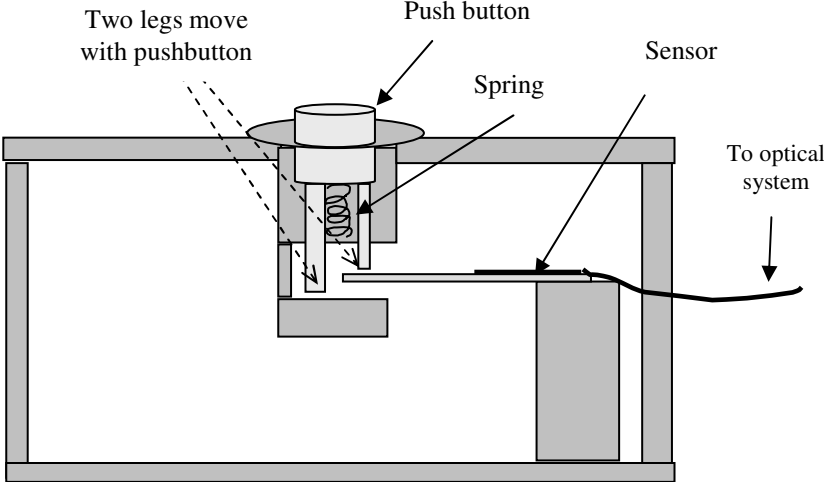


Fig. 6. Binary fiber optic switch

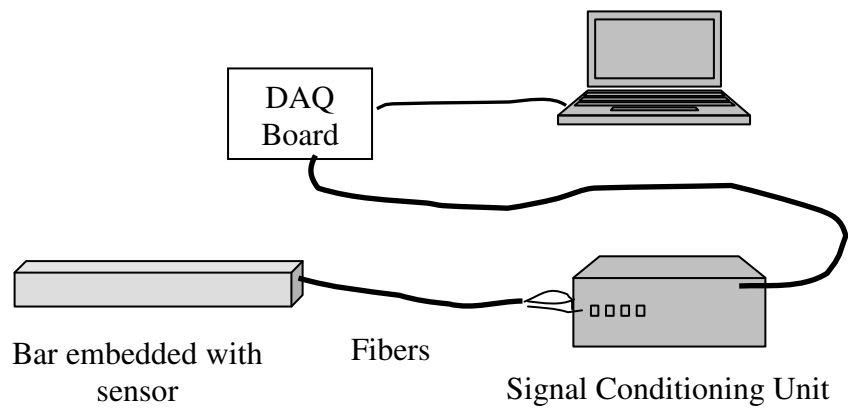


Fig. 7. FFPI weigh-in-motion measurement system

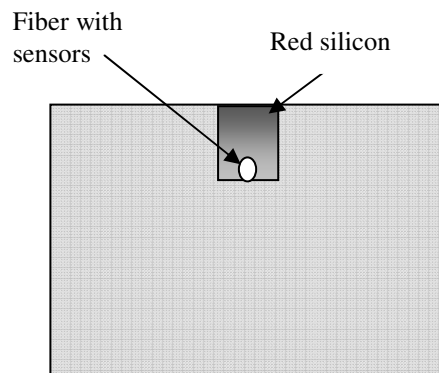


Fig.8. Cross section of metal bar embedded with fiber FFPI sensor

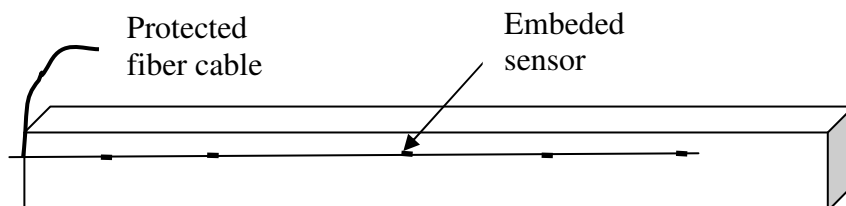


Fig 9. Sensors embedded in metal bars

3.3 Components Used in the Research

3.3.1 Light source

In this research two types of light source were used. One was superluminescent diode (SLD) with a peak wavelength of 1325nm, and one was distributed feedback (DFB) laser with a peak wavelength of 1554nm.

The SLD is a semiconductor laser which has the advantage of a broad bandwidth (typically a few tens of nm), which thus makes it a suitable light source for an LCI. It's less susceptible to reflection-induced noise than the high coherence laser diodes. The elimination of the reflection from the diode surface is the main difficulty in the manufacturing of an SLD. There are several methods to suppress lasing such as unpumped absorbing regions [30] and window structures with tapered active layers [30, 31]. The characteristics of the SLD are given in Table 1.

Table 1. Optical and electrical characteristics of SLD

Parameter	Symbol	Condition	Min	Typical	Max	Unit
Fiber output power	P	cw	0.5	--	2	mW
Peak wavelength	λ_p	cw	1330	1350	1380	nm
Spectral width	$\Delta\lambda$	cw	20	30	40	nm
Operating voltage	V_p	cw	1.3	1.5	1.7	V
Operating temperature	T_c	cw	-40	--	+60	°C
TE cooler current	I_{TE}	cw	--	--	0.3	A
Bite rate	B	--	--	--	560	--
Lifetime	T_{life}	--	--	--	150	kH

The first report of a CW operation of a semiconductor DFB laser was made around the mid 1970s. Ordinary semiconductor lasers oscillate in many modes and are impossible to incorporate into a monolithic device. The DFB laser diodes were the only LDs with sufficient single-mode stability, sufficient modulation bandwidth and sufficient easy fabrication for use in today's optical communication systems. They have a corrugated layer etched internally, which forms an optical grating that selectively reflects light according to its wavelength. The grating period d is chosen to satisfy the Bragg condition $2n_{\text{eff}}d=\lambda$. In addition to their narrow bandwidth (typically 0.1-0.4nm) and long high-bandwidth transmission paths, DFB lasers are less temperature dependant and more linear in their response than conventional laser diodes. The characteristic of DFB's are given in Table 2.

3.3.2 Photodetector

We used three Fujitsu FID3Z1LX InGaAs PIN photodectors with multimode fiber pigtails in our setup. PIN photodiodes are the most common detectors in fiber systems. The PIN diode has a wide intrinsic semiconductor layer with a high resistance between the p and n regions; this improves the efficiency and the speed relative to the pn photodiode. The photodiodes we used were designed for use in high bit rate transmission systems up to 2.5GB, and local area network and subscriber loop at both 1310nm and 1550nm wavelengths. The PIN chip has a photosensitive area of 50 μ m in diameter, with a planar structure and a guard ring for high reliability. The quantum efficiency is specified to be over 80% at 1310nm and the dark current is 0.1nA, both at room

Table 2. Optical and electrical characteristics of DFB laser

Parameter	Symbol	Condition	Min	Typical	Max	Unit
Fiber output power	P	cw	2.0	--	--	mW
Threshold current	I_{th}	cw	2.0	--	50	mA
Forward current	V_f	cw, P=2.0mW		1.1	1.5	V
Slope efficiency	S	cw, P=2.0mW	33	--	200	μ W/mA
Modulation current	I_m	cw, P=2.0mW	10	--	60	mA
Peak wavelength	λ_p	cw, P=2.0mW	1530	--	1570	nm
Spectral width	$\Delta\lambda$	cw, P=2.0mW	--	--	0.4	nm
Sidemode suppression		cw, P=2.0mW	30			dB
Monitor current	I_m	cw	0.05	--	1.0	mA
Monitoring dark current	C_D	cw	--	1	500	nA
Monitor capacity	C_t	f-1MHz	--	6	10	pF
Linearity of P- I_m		cw	--	--	± 10	%

temperature and with a reverse voltage of 5K. The optical and electrical characteristics and the maximum rating of the photodiode are listed in Tables 3a and 3b.

3.3.3 Translation stage and motor control system

In our LCI systems, the mechanical scanning of the Michelson interferometer is controlled by a motorized micropositioning system to provide the scanning of the mirrors. A micropositioning system consists of the actuator and the driver.

The Motor MikeTM actuator by Oriel Corporation uses a DC motor with an integral gear head to allow pinpoint positioning or constant velocity operation. The

Table 3a. Absolute maximum rating of the photodetector

Parameter	Symbol	Rating	Unit
Storage Temperature	T_{stg}	-40 to+90	°C
Operating case temperature	T_{op}	-40 to+90	°C
Forward current	I_F	5	mA
Reverse current	I_R	2	mA
Reverse Voltage	V_R	20	V

Table 3b. The optical and electrical characteristics of the photodetector

Parameter	Symbol	Condition	Min.	Max.	Unit
Responsibility	R	$V_R=1V, 1300nm$	0.8	---	A/W
		$V_R=1V, 1500nm$			A/W
Variation of Responsibility	ΔR	$V_R=1V, -20\text{--}+70^\circ C$	---	± 3	%
		$V_R=1V, -40\text{--}+85^\circ C$	---	± 4	%
Dark current	I_D	$V_R=5V, T_a=25^\circ C$	---	1	nA
		$V_R=5V, T_a=70^\circ C$	---	10	
		$V_R=5V, T_a=25^\circ C$	---	20	
Cut-off frequency	f_c	$R_L=50\Omega, V_R=5V$	2.5	---	GHz
		-3dBfrom 500kHz			
Capacity	C_t	$F=1MHz, V_R=5V,$	---	0.9	pF
Optical return Loss			30	---	dB

travel length is 50mm, an inch and metric scale provides a coarse reading of the spindle's travel. It provides high resolution and minimal backlash.

The driver we used is a DCX-PCI100 Intel compatible PC computer-based servomotor and I/O controller made by Precision MicroControl (PMC). The DCX-PCI100 Motion Controller provides drive and control signals for 1 to 8 miniature DC servo motors, eliminating the cost and bulk of external amplifiers for these motors. This controller is based on PMC's field-proven modular multi-processor architecture and is designed to control high-precision, low-power motorized micrometer actuators and stages in applications such as opto-electronic R&D and production, medical and scientific instrumentation, and laboratory automation.

The DCX motherboard uses a 192MHz 32 bit MIPS processor that is programmed to perform motion control tasks. Specially designed servo control nodules were installed on the motherboard to configure it for controlling from 1 to 8 servo motors. Each DCX motion control module installed on the motherboard provides all the circuitry required to control on the motor and its associated axis I/O.

The DCX servo modules use a position feedback loop to control the servo. The DCX-MC100 controls the operation of the servo motor via a 12 bit, +/- 10volt analog output signal to an external servo amplifier. It provides a 0-12volt, 8 bit, direct motor drive output capable of directly driving a 12 volt motor with up to 0.5A of current.

Incremental encoder inputs to these modules provide the feedback information for closing the position loop. In operation, the servo module subtracts the actual position (the feedback position) from the desired position (the trajectory generator position), and

the resulting position error is processed by the digital filter on the module. The output of the digital filter sets the module's servo command output level.

The module processor monitors the motor's position via an incremental encoder. The two quadrature signals from the encoder are used to keep track of the absolute position of the motor. Each time a logic transition occurs at one of the quadrature inputs. The DCX position counter is incremented or decremented accordingly. This provides four times the resolution over the number of lines provided by the encoder. The encoder interface is buffered by a differential line receiver on the DCX module. Jumpers on the DCX module allow the user to configure the differential receiver for use with single ended or differential encoders.

A "Proportional Integral Derivative" (PID) digital filter on the module is used to compensate for the servo feedback loop. The motor is held at the desired position by applying a restoring force to the motor proportional to the position error, plus the integral of the error and the derivative of that error.

3.3.4 The Signal Conditioning System (SCU)

The SCU is manufactured by Fiber Dynamics Incorporation and is designed for 8, 12 or 24 channels; it is mainly composed of three parts: the sensor, the Signal Conditioning Unit and a Hand Held Terminal (HHT) control for configuration of the system, shown in Fig.10. (from manual of SCU). The Signal Conditioning Unit has a 1.3 μ m DFB laser installed in it, along with a thermoelectric cooler (TEC) for stable temperature operation. The laser is driven with a current driver (CD) and modulated with

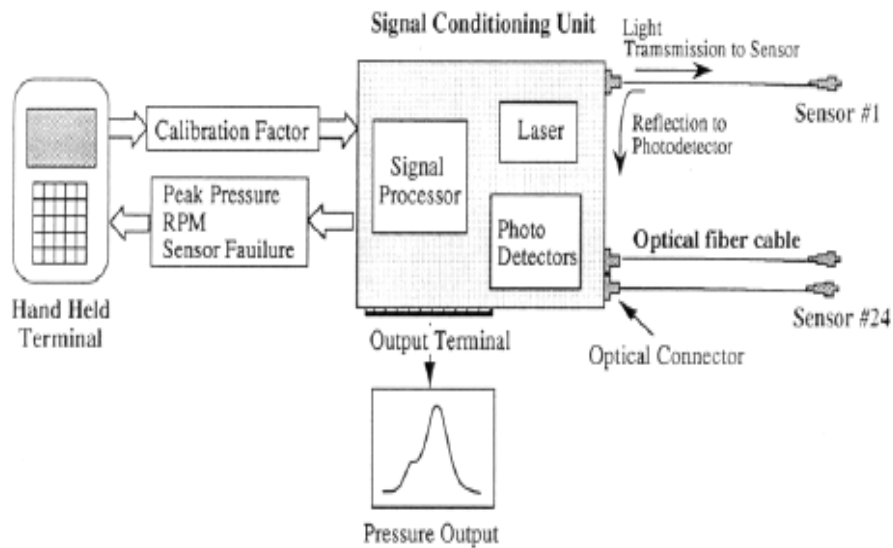


Fig. 10. Structure of Signal Conditioning Unit (SCU) for 24 channels

a periodic waveform by a microprocessor. An optical splitter (or coupler) distributes the laser light to the individual FFPI sensors, and 8, 12 or 24 (the number of the channel) 2X1 splitters direct the reflected light to any array of photodetectors corresponding to each other. The optical system schematic is shown in Fig. 11.

After the reflected laser light from each sensor is converted to an electrical signal by the photodiode, a microprocessor tracks the signal change by using a digital timing scheme to determine the optical phase shift in each sensor. The signal is analyzed with a comparator and the perturbation information is passed to the output terminal. One reference FFPI is used to compensate for any wavelength drift of the laser and linearity of the system. The normal sampling rate is 2.4 kHz, equal to the repetition frequency of

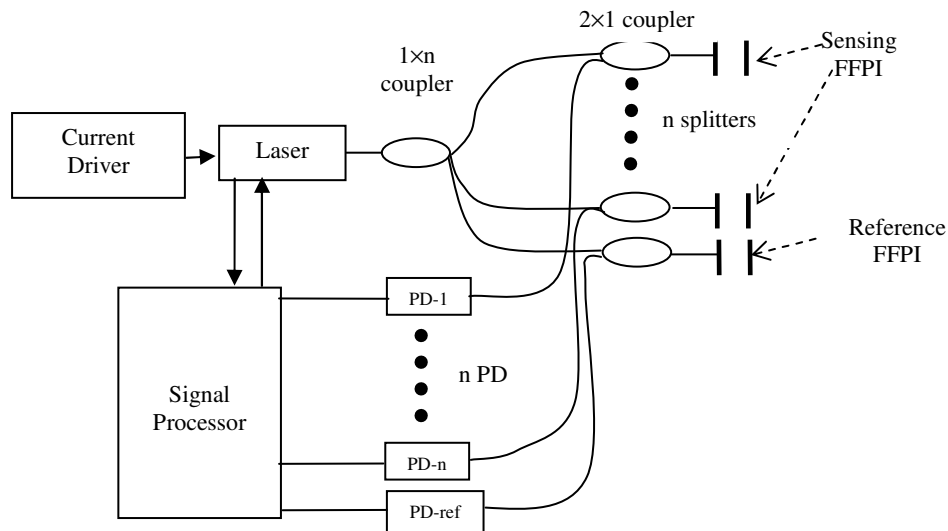


Fig. 11. Optical system schematics of SCU

the laser. The sampling rate can be increased to 8 kHz through the HHT, with a corresponding reduction in the number of active channels.

3.3.5 Falling Weight Deflectometer (FWD)

The field testing and calibration of the WIM systems were developed based upon a falling weight deflectometer. The falling weight deflectometer (FWD) (shown in Fig. 12) is an impulse-type testing device that produces a dynamic, transient impulse load on the pavement surface that simulate a moving wheel load. The duration and magnitude of the force applied is representative of the load pulse induced by a moving truck or aircraft at moderate speeds. Measurement of the pavement's structural properties via the FWD is a commonly accepted practice in highway pavement testing with the advantage of nondestructive, one man operation, accurate and fast, with a wide loading range and is easily transportable [3][32].

The FWD provides us all the necessary information such as load impact, surface deflection, and deflection in different depth, etc. The emphasis of the test was placed on the repeatability of the FWD results, the linearity of the load impact with corresponding sensor signal output, and estimate of the unknown load and the sensor signal amplitude variations with the various load positions.

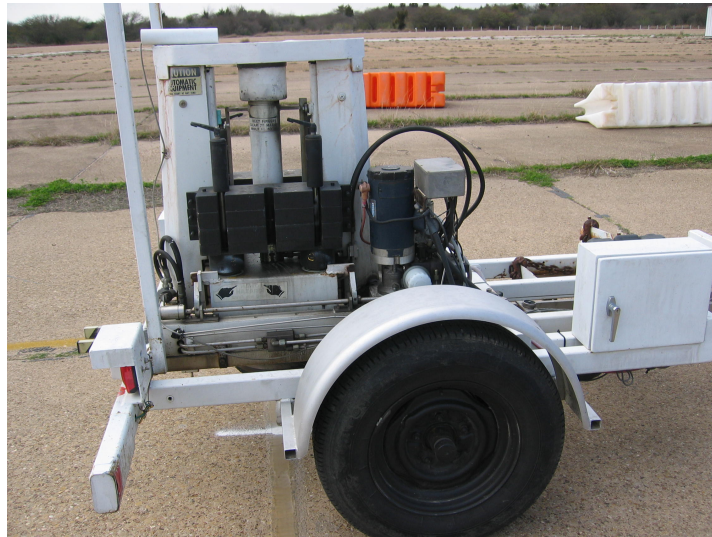


Fig. 12. Falling weight deflectometer

CHAPTER IV

SIGNAL PROCESSING ALGORITHM

4.1 Summary of Signal Processing Algorithm

The collected data are two sets of interference fringes shown in Fig. 13. They are cosine waves modulated by a Gaussian profile: one fringe pattern for the sensing FFPI and another for a reference which is not subjected to strain. Three factors determine the accuracy of the WLI system: (1) the irregularities in the movement of the translation stage in Michelson processing interferometer (2) whether the central (maximum-amplitude) fringe can be accurately identified and (3) whether the peak position of the central fringe can be precisely determined.

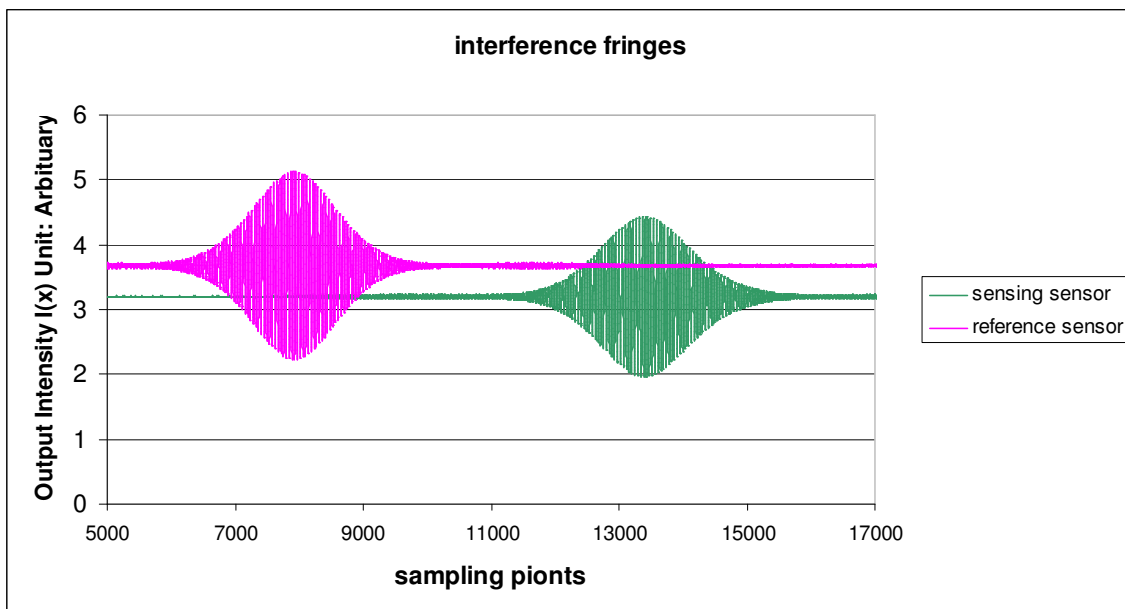


Fig. 13. Interference fringe patterns of sensing and reference sensors

The second Michelson interferometer driven by a DFB laser is critical to the setup here in order to achieve a high level of precision in the OPD measurement and to facilitate the multiplexing sensor measurements along one single fiber with high sensitivity. A unique signal processing algorithm implemented in C++ language has been developed at Texas A&M University to correct the velocity change in the translation stage, identify the central fringe, determine its precise position, and determine the state of the binary switch. Three major signal processing steps to be performed in the data processing procedure are:

(1). Correct the SLD fringe data using the DFB fringe data

This step corrects for changes in speed during the translation stage scans. The output from the DFB Michelson interferometer is assumed to be a sinusoidal function of the mirror displacement. The sinusoidal periodicity is determined by the very stable DFB laser wavelength, and thus can be assumed to be constant and can be used to control time to distance transformation of the data from the SLD processing interferometer. Therefore, it makes it possible to precisely determine the position of the moving mirror when its speed varies with time.

(2). Perform a cross correlation of the sensing fringe data, noted as $sen[i]$, and reference fringe data noted as $ref[i]$.

After cross correlation, the position of the central fringe represents the distance between the central peaks of $sen[i]$ and $ref[i]$. Because the amplitudes of the fringes near the central fringe are very nearly the same, reliable identification of the central fringe is

crucial. A mistake in the identification will result in a large measurement error and is intolerable.

(3). Determine the state of the binary switch from the central fringe position which theoretically is a linear response to applied force.

The National Instrument data acquisition board (AT-MIO-16E-1) and a specifically designed Labview program are used to collect analog input data from the photodiode. The sampling rate is 4000 sample/second, the collected data were saved in data files and later processed by the C++ program.

4.2 Correction of SLD Fringe Data Using DFB Fringe Data

First we needed to filter and normalize the sensor and reference data sets. Let sno denotes the sampling number

$$sen[i] = \frac{C_0 sen[i] + C_1 sen[i+1] + \dots + C_n sen[i+n]}{n+1} \quad (4.1)$$

$$ref[i] = \frac{C_0 ref[i] + C_1 ref[i+1] + \dots + C_n ref[i+n]}{n+1} \quad (4.2)$$

where n and $C_0 \sim C_n$ depend upon filter function. For a smoothing by 5 point average, $n=4$ and $C_i=1$ for ($i=1$ to n). After this, $sno=(original\ sno)-(4)$.

Then we performed a normalization to make the average values of both fringe data become zero

$$sen[i] = sen[i] - \frac{\sum sen[i]}{sno} \quad (4.3)$$

$$ref[i] = ref[i] - \frac{\sum ref[i]}{sno} \quad (4.4)$$

The fringe patterns shown in Fig. 13 are intensity versus time. In calculating the OPD, what we needed was intensity versus the temporal position, the periodicity of DFB laser signal is used as a criterion. The procedure can be concluded by the following 3 steps:

1. Zero-Point determination: precisely determine the points at which the DFB laser signal crosses the baseline using a linear interpolation of the sampled DFB interferometer signal. The baseline is set to be the average value of the DFB data set. The distance between the two adjacent zero-points indicate half-wavelength ($\lambda/2$) temporal displacement in the translation stage.
2. DFB grid construction: inserting a fixed number of points equally spaced between zero-points. In our experiments, we inserted 50 points per each half-wavelength in order to ensure enough sampling points and resolution.
3. Resample the sensor data: determine the value of the reference and sensing sensors signals at the time corresponding to the DFB grid by linear interpolation of the two adjacent original sampled signals. After resampling, the new set of data represents intensity versus temporal distance.

4.3 Perform Cross Correlation of New $sen[i]$ and $ref[i]$

The cross correlation of the resampled sensing and reference data is given by

$$cor[i] = \sum_{j=0}^{sno-1} ref[j] * sen[j+i] \quad (4.5)$$

for $-(sno-1) \leq i \leq (sno-1)$ and for $0 \leq (j+i) \leq (sno-1)$.

After cross correlation, the central fringe position of the correlation result represents the distance of the central fringe position of $sen[i]$ from that of $ref[i]$, which represent the optical path difference between the reference and sensing sensors.

Figs. 14 and 15 depict the experimental cross-correlation data before and after we used the correction by the DFB fringe. They clearly indicate the necessity and importance of using the DFB interferometer compensation to obtain precision OPD measurements with WLI techniques.

4.4 Identify the Central Fringe in Corrected Correlation Data

Fig. 16 shows that the peak points compose an envelop function. The identification of the central fringe pattern can be performed by hypothetic test using the following equation

$$\Delta(i, j) = E(i + j) - E(i - j) \quad (4.6)$$

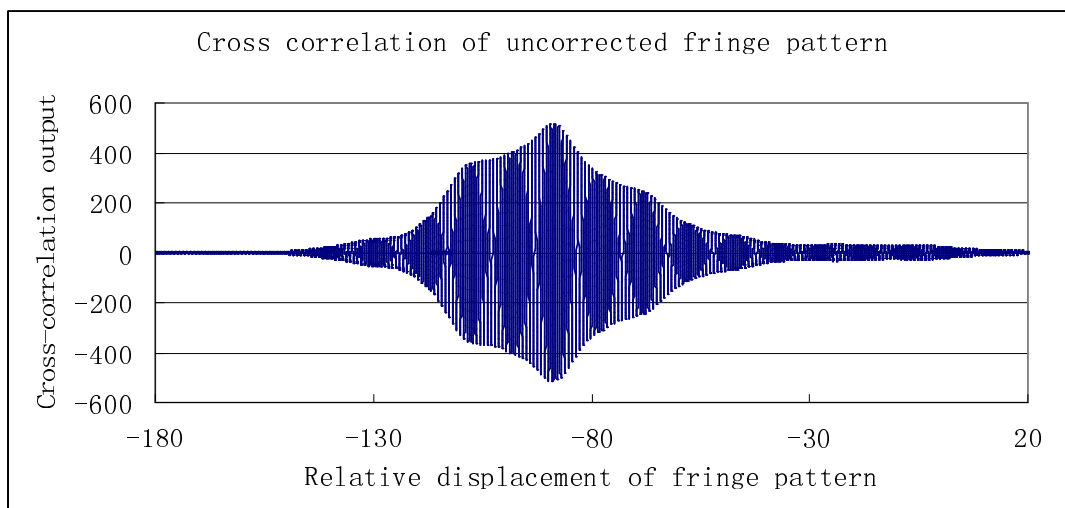


Fig. 14. Cross-correlation of fringe pattern before correction

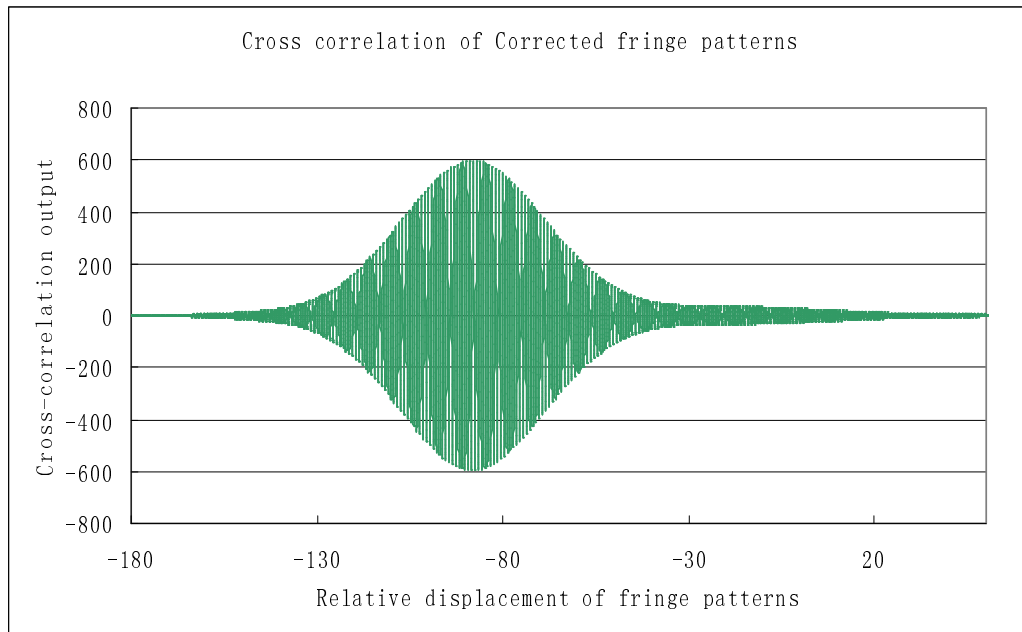


Fig. 15. Cross-correlation of fringe pattern after correction

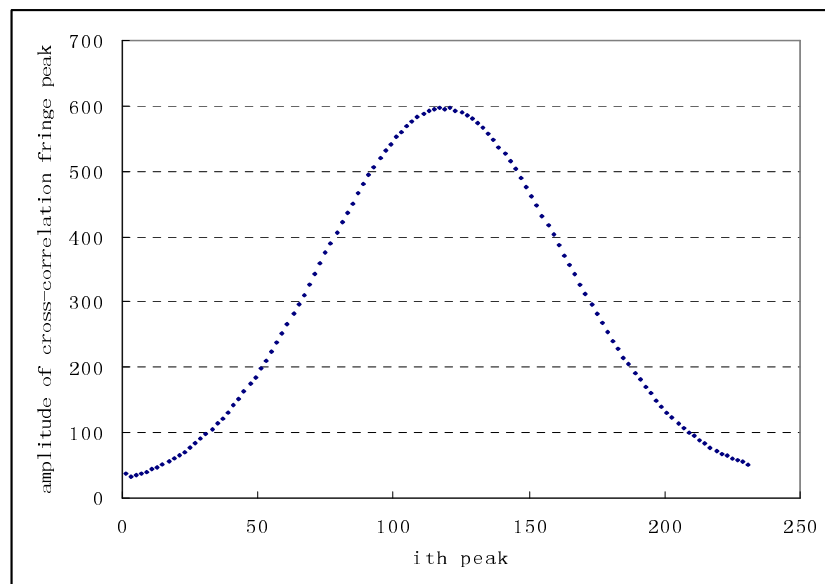


Fig. 16. The envelop of fringe peak of Fig. 15

where $E(i)$ is the i th peak amplitude of the correlation data, in an ideal noiseless case, and $\Delta(i_c, j)$ will be zero for all j if i_c is the central fringe. In lab tests, we assumed that the minimum values of summation of all $\Delta(i, j)$ through j corresponded to the central fringe.

The central fringe is then correlated with a set of true cosine curve generated by computer for enhancement of the resolution [28]

$$re_sum[i] = \sum_{j=0}^{rcpn-lcpn} cor[lcpn + j] \cdot \cos\left[\frac{2\pi}{zcp}(lcpn + j) - cpnn - 1 + \frac{i}{F}\right] \quad (4.7)$$

where $lcpn$ and $rcpn$ are the indexes of the right and left negative peaks of the central fringe, $cpnn$ is the index of the central peak, and F is the resolution enhancement factor. The value of i which gives the maximum value of $reso_sum[i]$ corresponds to the enhanced central fringe position with an enhancement of

$$cpn_f = cpn + \frac{i - F}{F} \quad (4.8)$$

The C++ program for the whole data processing is listed in the Appendix.

CHAPTER V

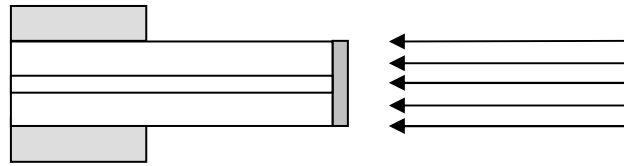
OPTICAL BINARY SWITCH EXPERIMENTAL PROCEDURE AND RESULTS

5.1 FFPI Sensor Fabrication

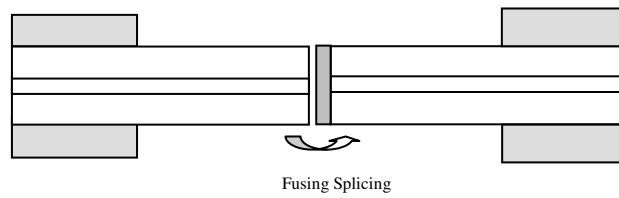
The fabrication procedure of the FFPI sensor is depicted in Fig. 17: (1) A magnetron sputtering machine is used to coat the cleaved fiber end with a thin film of TiO_2 of thickness 1000\AA . (2). Fusion splicing the coated fiber with a normal cleaved fiber. The splicing machine heats the cleaved surface of the fibers with an electric arc, and splices them together. By controlling the arc current and arc duration time (lower than a normal splice), the coated fiber and the normal fiber will form an in-line fiber with an internal mirror. Desired mirror reflectance and splicing strength can be achieved by multi-splicing. (3) The fiber with the mirror is then cleaved to the desired cavity length of 10mm or 12mm, and fusion spliced with another normal fiber. Again, multi-splicing of the joint achieves the desired mirror reflectance and splicing strength.

An experimental setup (Fig. 18) is used to monitor the FFPI fabrication. A $1.3\mu\text{m}$ DFB laser diode is driven by an LD driver circuit and modulated by a pulse generator. Light from the DFB laser passes through an isolator and a 3 dB coupler, and part of the signal is reflected from the sensor. The reflected signal then goes through the coupler to the photodiode. The reflection interference fringe is displayed on an oscilloscope (Fig 19).

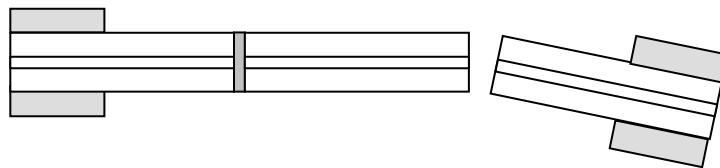
1. Sputtering TiO₂ on the cleaved fiber end



2. Fusion splicing to make the first mirror



3. Cleaving the desired cavity and fusion splicing with another coated fiber



4. Second mirror making complete the FFPI

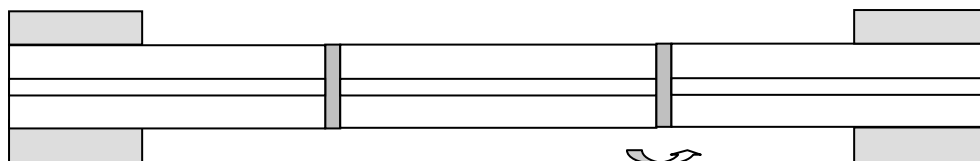


Fig. 17. FFPI sensor fabrication

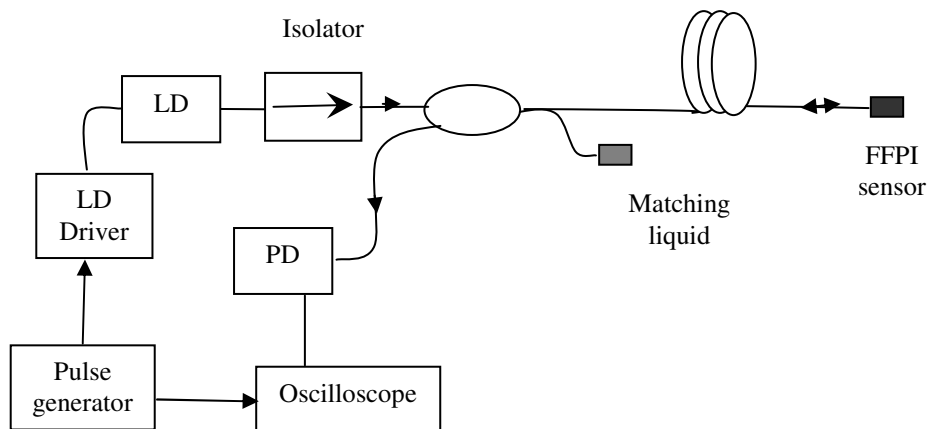


Fig. 18 Arrangement of monitoring the fabrication of FFPI

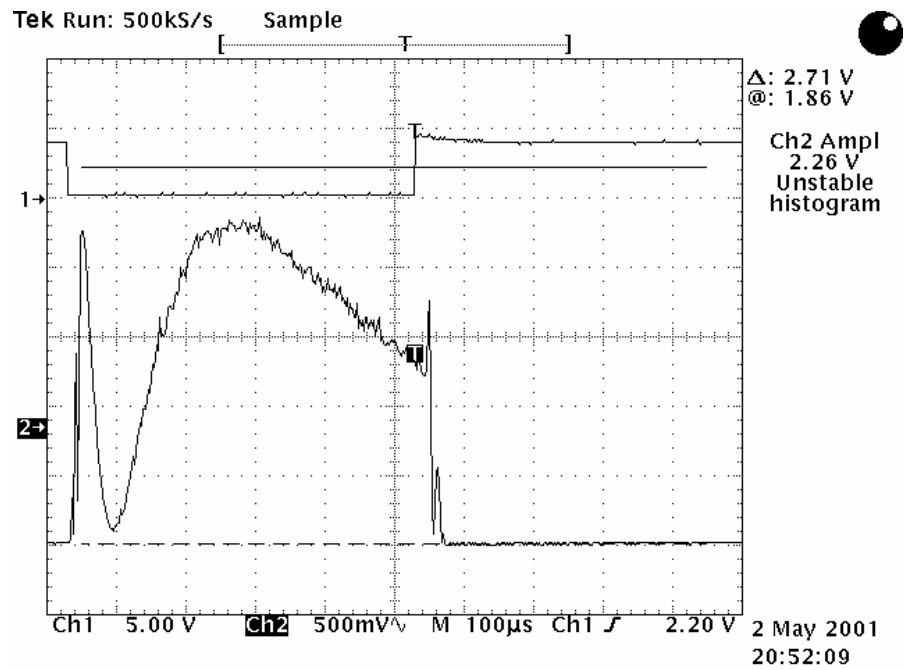


Fig. 19. Reflected sensor signal displayed in the oscilloscope

5.2 Optical Binary Switch System Overview

The sensing sensor is bonded to the copper cantilever as shown in Fig. 5, The reference sensor is free from stress and located in the same optical table to experience the same temperature. The FFPI cavity is around 10mm with a reflectivity of 0.05.

We used Ohaus metric weights to calibrate, as shown in Fig 5. The weight we added to elongate the cantilever ranged from 0 to 200g and 300g. The data was collected through the National Instrument PCI-MIO-16E-1 data acquisition board and via LabVIEW programming, and then processed by the C++ program. The sampling rate was kept at 4000/s by controlling the moving speed of the DC step motor at about 130 μ m/s. As a result, we achieved about 40 sampling points in one fringe, each of which was 1.32 μ m, the wavelength of the SLD.

The ILX Lightwave LDX-3412 current source was used to control the driving current of the SLD. Another LDX3525 current source was used to control the cooling current in the SLD package; the temperature of the SLD heat sink was sensed by an inner thermistor with a resistance of 15 Ω and monitored by a digital multimeter.

5.3 System Evaluation

5.3.1 Signal Noise Ratio (SNR) of the system

The signal-noise-ratio (SNR) was tested to evaluate the possibility of correctly identifying the central fringe. The noise was calculated as follows

$$V_{noise} = \sqrt{\frac{\sum_{n=0}^{N-1} [V(n)]^2}{N}} . \quad (5.1)$$

Here N represents the total sample points collected in calculating the SNR, $V(n)$ is the n th noise data, and the SNR is:

$$SNR = 20 \log \frac{V_{signal}}{V_{noise}} \quad (5.2)$$

Most of the noise comes from a lab-made signal amplifier. If using a commercial low-noise signal amplifier; the SNR can be reduced 18 dB lower. Additional noise may be induced by the effect of temperature on the photodetector, light scattering in the optical setup and the overall data acquisition process. Previous researches have concluded that even at low SNR conditions for the system, the system still works well. In our experiments the driven current of the SLD is usually within 180-198 mA. For all the tests conducted, the measured SNR of reference and sensing sensor were all over 40dB.

5.3.2 Resolution test

Two resolution tests were performed to evaluate the system. The first test was the resolution of the optical WLI system. The sensing sensor was free from bonding to the cantilever and both the sensing and reference sensors were kept at the same temperature. The experiment's results are shown in Fig. 20. This shows that the maximum fringe drift (maximum minus the minimum fringe) is 0.0022 fringes, and the standard deviation is 0.000651. The second resolution test tested the whole optical binary system. The sensing sensor was bonded to the cantilever with no weight added in order to compare it to the first test; also, the two sensors were kept at the same temperature. The experiment's results are shown in Fig. 21. The maximum fringe drift is 0.025 fringe, and standard

deviation is 0.007029. There was a recorded 10 times difference in resolution, which possibly originates from the uneven residual stress in the bonding process and mechanical vibration of the cantilever. The resolution can be increased by improving the mechanical fabrication process in the optical binary switch.

From equation (3.2), with Young's Modulus $E=130\text{GPa}$ for the copper, cantilever represented as $L_b=50\text{mm}$, $b=2\text{mm}$, $h=4\text{mm}$, and the sensor cavity at $L=10\text{mm}$, the elongation of the cavity ΔL is $0.006329\ \mu\text{m}/\text{gram}$, corresponding to a 0.01104 fringe displacement/gram. Thus the resolution in applied weight is recorded as 2.3g . Spatial resolution when the wavelength is 1320nm is 33nm .

The main element in the optical system that degrades the optical system's resolution is the stabilization of the DFB laser wavelength. The drift of the wavelength within a single data acquisition period will induce changes in the DFB zero-crossing periods, and thus will cause error in signal processing. The wavelength of the DFB laser is affected by both the drive current and the laser case temperature. These two parameters must be held constant during the experiment. The DFB laser that we used changes the wavelength 5nm when the temperature changes about 40°C , which corresponds to 0.125nm per $^\circ\text{C}$. Another possible element is the SLD power fluctuation caused by the changes in power supply; which has been shown to have a minor influence.

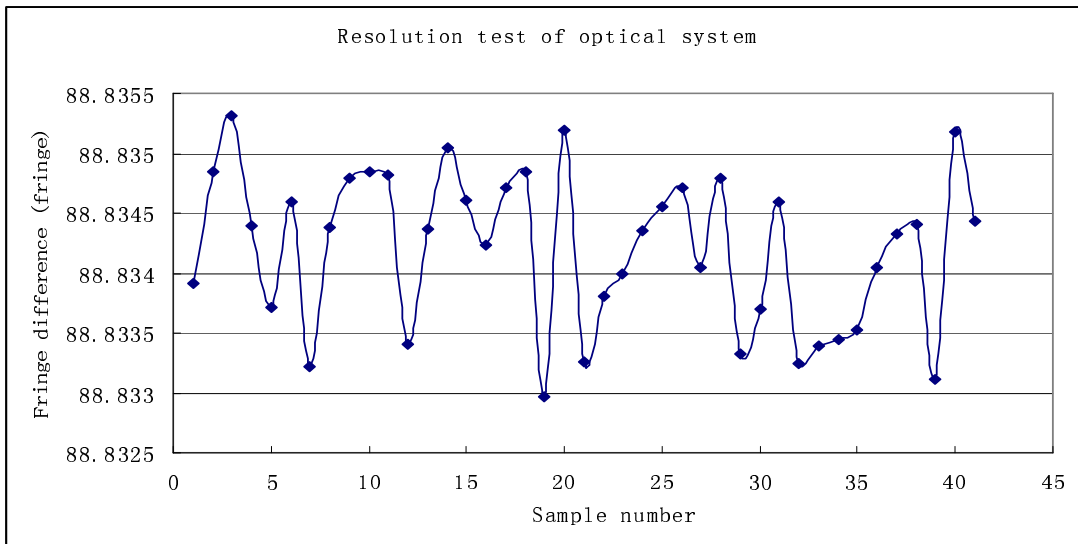


Fig. 20. Resolution test of the optical system when the sensing sensor is free from bonding to the cantilever

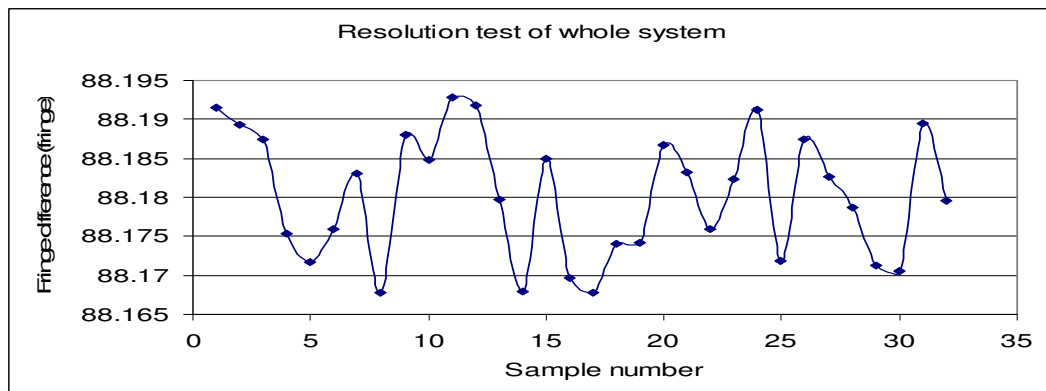


Fig. 21 Resolution test of the whole system when the sensing sensor is bonded to the cantilever

5.3.3 Binary switch calibration, repeatability and threshold determination

A series of calibration and repeatability tests were carried out using the setup in Fig. 5. Two example test results are shown in Fig. 22 and Fig. 23 using two different

sensing sensors (cavity length 10mm) and the same reference sensor. We used $Y=X_0+\alpha*G$ to describe how the fringe displacement varies with the added weight, where G is the added weight, Y is the fringe displacement after applying the weight, X_0 is the initial 0g fringe displacement, and α is $\Delta Y/\Delta G$. In Fig. 22 the weight was increased from 0 to 294g, and then decreased to 0g. The α factor for the increases in weight is 0.01188 fringe/gram, and the α factor for the decreases in weight is 0.01163fringe/gram. In Fig. 23 the weight was increased from 0 to 200g and then decreased to 0g. The α for the increases in weight is 0.01162, the α for the decreases in weight is 0.01128. Theoretical α result has been obtained to be 0.01104; the experimental results are in good agreement with this theoretical value. The tiny difference probably originated from measurements of the following parameters: the cavity length of the sensors, and the length, width and height of the cantilever.

The results show that the fringe displacement was a monotonic and good linear function of the applied weight, with a calibration factor of one fringe per 90 g of force applied, and little hysteresis was observed. In the present avionics application, the threshold could be set at any value less than 200 g, the minimum force applied by a pilot seeking to actuate the switch.

The Binary Optical Switch design has already been shown in Fig. 6. The push button is supported by a spring to ensure that the cantilever is free from any contact. When it is pushed, the shorter leg applies force to the cantilever, while the longer leg protects the cantilever from being over-bended in case the pushing force is too strong.

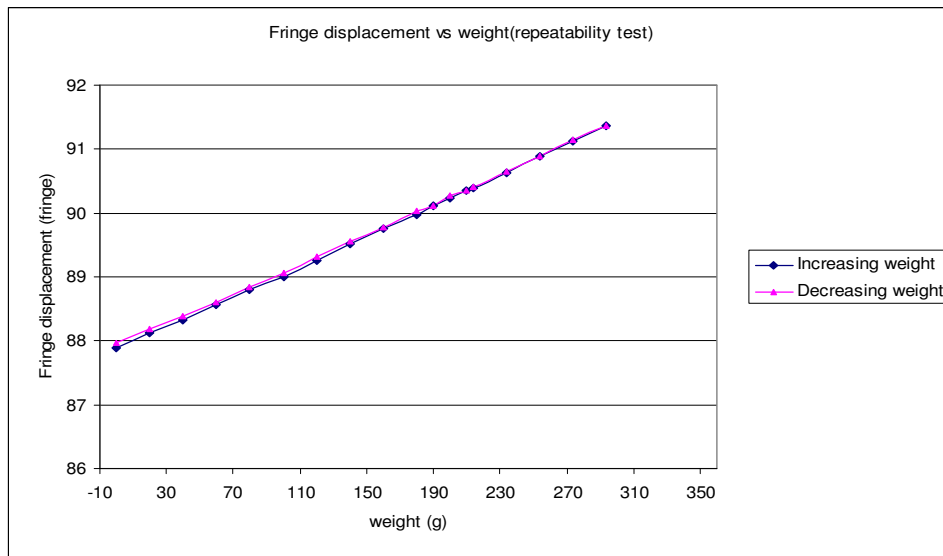


Fig. 22 Calibration and repeatability test of the binary switch (sensor #1)

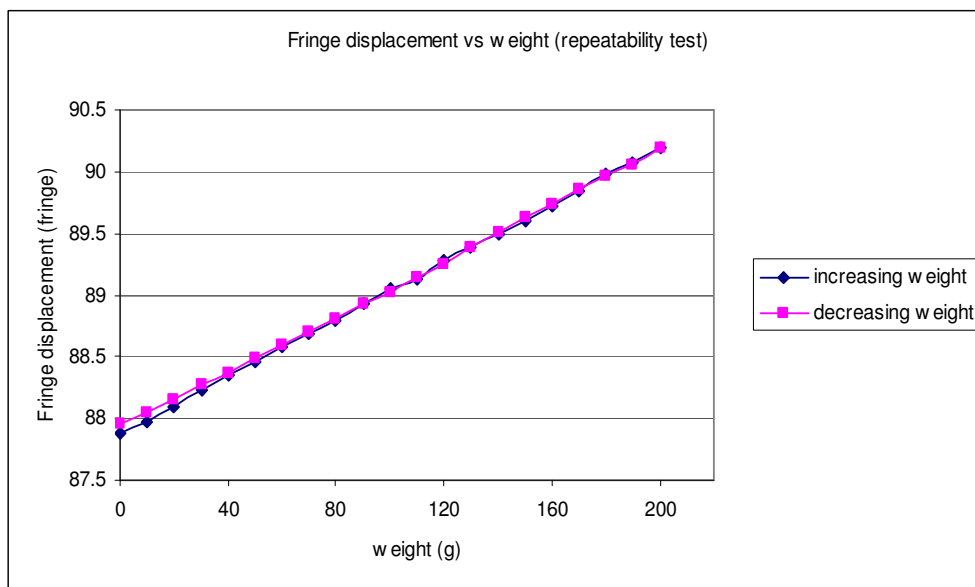


Fig. 23 Calibration and repeatability test of the binary switch (sensor #2)

The threshold of applied weight was set to be 100g in our test, and the initial value of X_0 was tested when no force was applied to the cantilever. Then the threshold of output signal is determined. For example, in sensor #2, $X_0=87.89$, $b=0.01162$, from calculations the threshold of fringe displacement was set to $Y_t=89.1$. With no failure recorded, the binary switch successfully produced a “1” output whenever the button was pushed and a “0” when there was no force.

CHAPTER VI

FIBER OPTIC WEIGH-IN-MOTION SENSOR EXPERIMENTAL PROCEDURE AND RESULTS

6.1 Laboratory Characterization Tests and Results

Laboratory tests on the performance of the embedded FFPI sensors were performed in the Texas Transportation Institute (TTI) Material Testing System (MTS) laboratory. The test samples were 1 foot long aluminum and steel bars, with an FFPI sensor embedded in the center of each bar. In each case the axis of the FFPI sensing fiber was parallel to the axis of the metal bar. During each test sequence, the MTS machine strikes the bar five times at a 5 Hz frequency. The maximum applied force can be varied from 200 to 4500 pounds, with a minimum of 50 pounds exerted in every strike to eliminate any bouncing of the bar.

The response of the sensors embedded in the steel and aluminum with a maximum MTS striking force of 2000 pounds are shown in Figs. 24 and 25. The signal for the sensor embedded in the steel bar showed a single peak in response to an MTS strike, while the aluminum bar exhibited a pronounced ringing effect with two strain peaks for each strike. Figure 26 shows the axial displacement of the steel bar and the fiber-optic sensor response as a function of the maximum MTS force. The axial displacement data was obtained with a conventional sensor (data provided by TTI). Both the axial displacement and the fiber-optic sensor's amplitude are nonlinear functions of the maximum force. However, as shown in Fig. 27, the fiber optic sensor's

response is a fairly linear function of the axial displacement, indicating that this sensor is a promising solution for measuring strain in the WIM application.

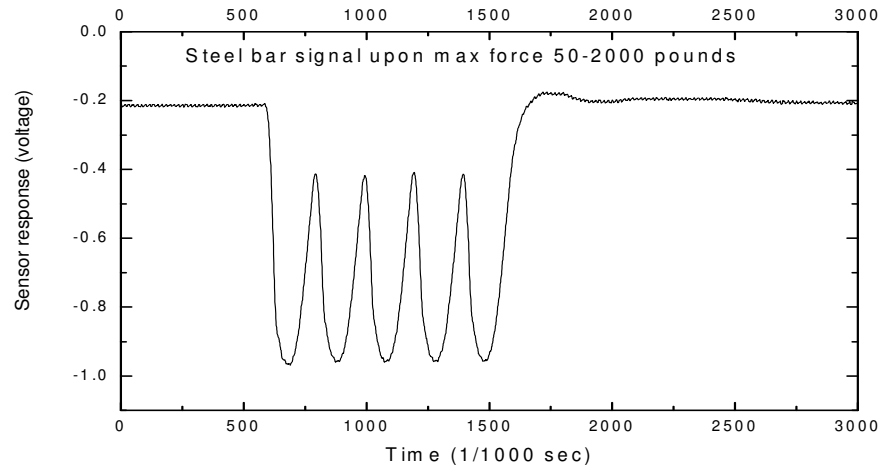


Fig. 24. Steel bar response to the MTS

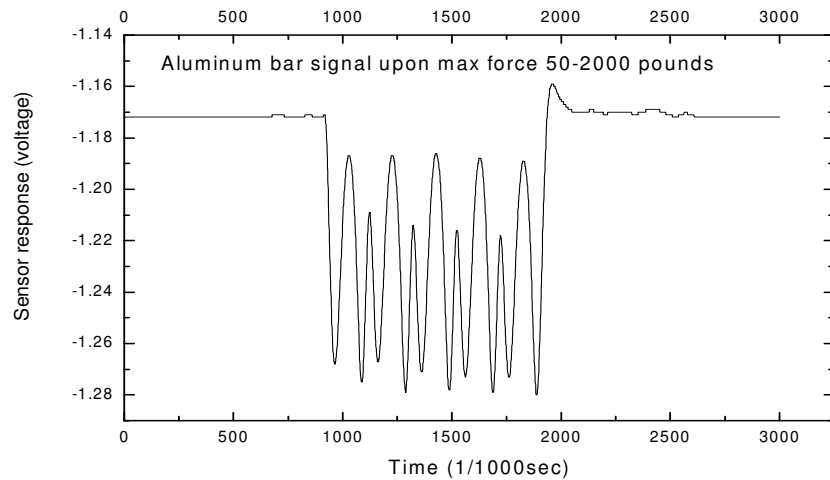


Fig. 25. Aluminum bar response to the MTS

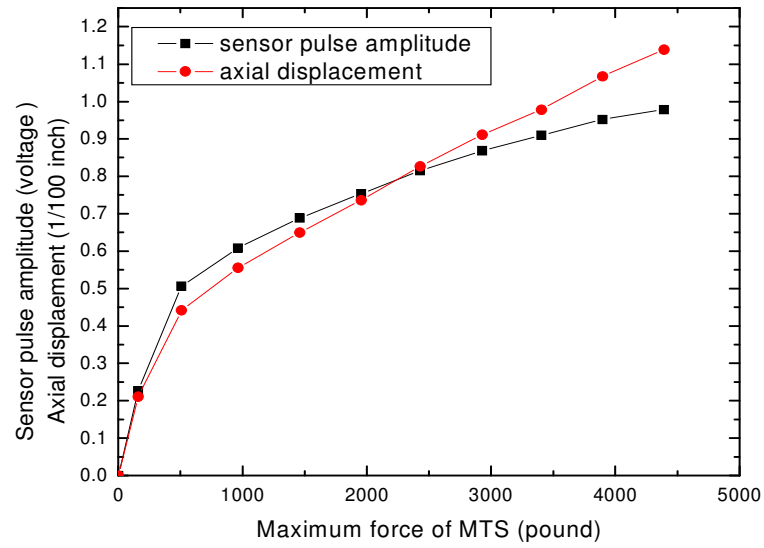


Fig. 26. Dependence of the peak FFPI sensor response and axial displacement on a striking force

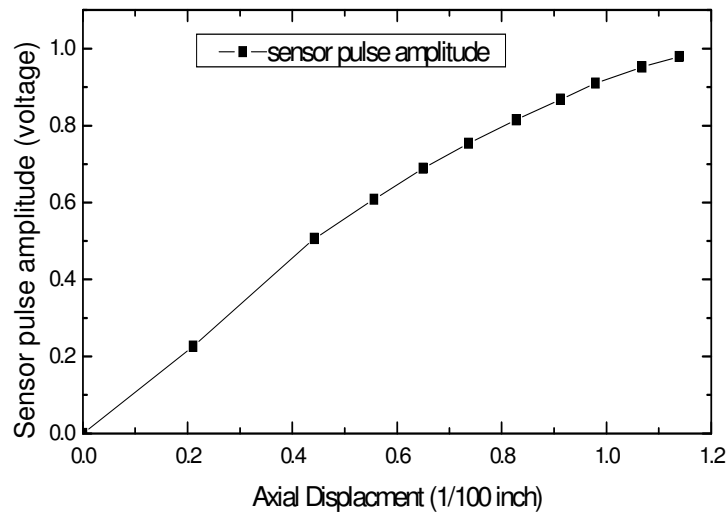


Fig. 27. Dependence of the peak FFPI sensor response on the axial displacement

6.2. Highway Tests and Results

Road tests were performed in August 2003 on Texas SH48. As in the MTS tests, the sensors were embedded in steel and aluminum bars with cross-sectional dimensions of 1 x 1 inch. In the road tests, the bars were 4 feet long, and 5 sensors were embedded in each bar, as shown in Fig. 28. The distribution of the sensors was intended to ensure that the right side tires of the truck will pass close to one or more of the sensors. Two saw cuts were made in the freeway across half of one lane, 1 inch wide and 2 inches deep. Hot bituminous sealant was used to secure the bars into the roadway and fill in the sawed grooves. After the bar was bonded into place, solid hot mix Epoxy was used to evenly fill in the grooves to the level of the road surface, so that the sensors measured the strain experienced by the surrounding pavement.

Representative data are shown in Figs. 29 and 30. Because the signal amplitude is based on the position of the wheels relative to the sensor, the relative amplitudes are an indication of the position of the truck in the lane. In Fig. 29, sensor 5 produces a signal larger than that of the other sensors, indicating that the truck is in the right-hand portion

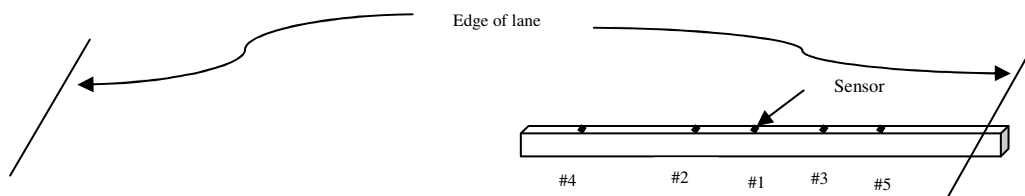


Fig. 28. Locations of the sensors, in inches, along the four foot length of a metal bar.

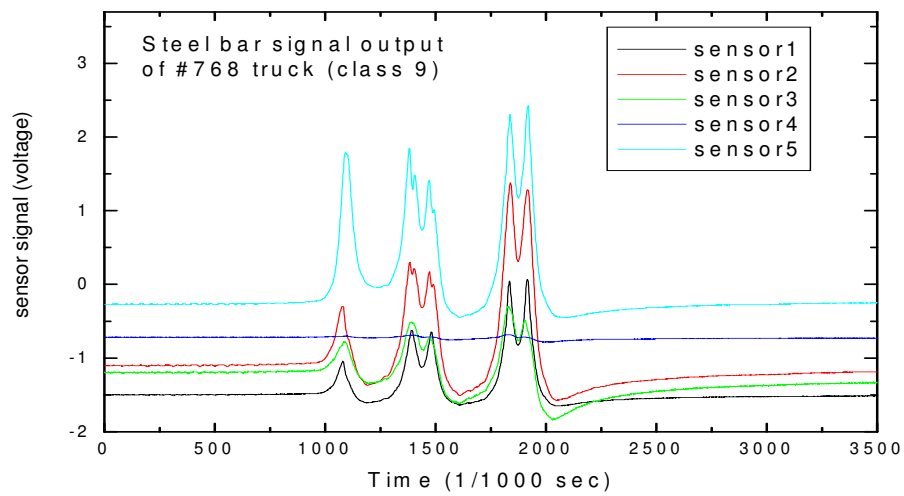


Fig. 29. Response of five FFPI sensors embedded in the steel bar to a class 9 truck, as distinguished by two wheel crossings in the third group

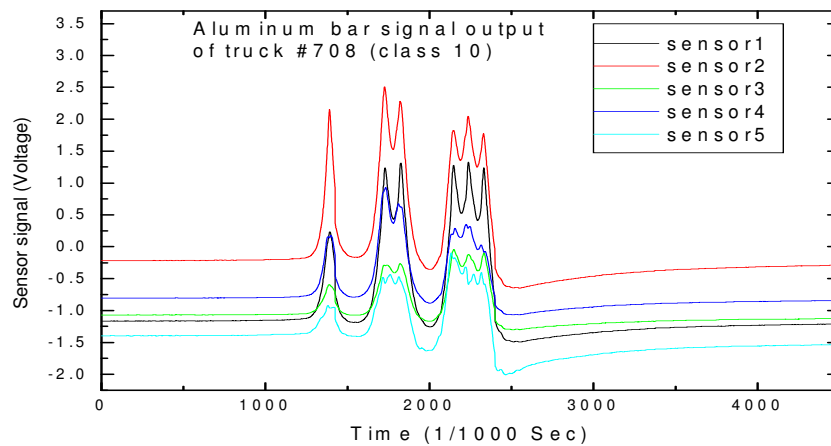


Fig. 30. Response of five FFPI sensors embedded in the aluminum bar to a class 10 truck, as distinguished by three wheel crossings in the third group

of the lane. After a truck passes by, the signal from each sensor quickly resumes its starting value, thus allowing for the collection of data from a continuous line of trucks.

A total of 30 trucks were monitored with sensors in the aluminum bar and another 30 trucks were monitored with sensors in the steel bar. An effort to correlate the fiber optic sensor data with the static weights of these trucks supplied by TTI was not successful. One factor which probably contributed to the discrepancy was the fact that the limited distance (2 ½ feet) over which the FFPI sensors were distributed made it possible to monitor only one wheel of each truck, so that uneven lateral distribution of weight would lead to erroneous readings.

6.3 FFPI Weigh-In-Motion System Installation at the Riverside Campus

The FFPI sensor was bonded with polyimide in a 1/4×1/8 inch groove in the 5 feet long metal bar as shown in Fig. 8. The extended fiber cables were total 250 feet long and had an FC-APC connection to the SCU for signal acquisition and processing. The cable was protected from bending by ~1 meter shrinkage tube at the very end of the metal bar. Sensors were embedded in both the steel and the aluminum bars in order to compare the performance of the two materials under each truckload. The lengths of the bars were 5 Feet. In total 5 sensors were embedded in each bar.

Two steel bars and two aluminum bars were each embedded with 5 sensors and installed in two lanes on the flight line road between 6th and 7th street at Texas A&M's Riverside campus. The proposed WIM Riverside project layout is shown in Fig. 31. Four saw cuts were made in the concrete road to house the four metal bars and fibers cables.

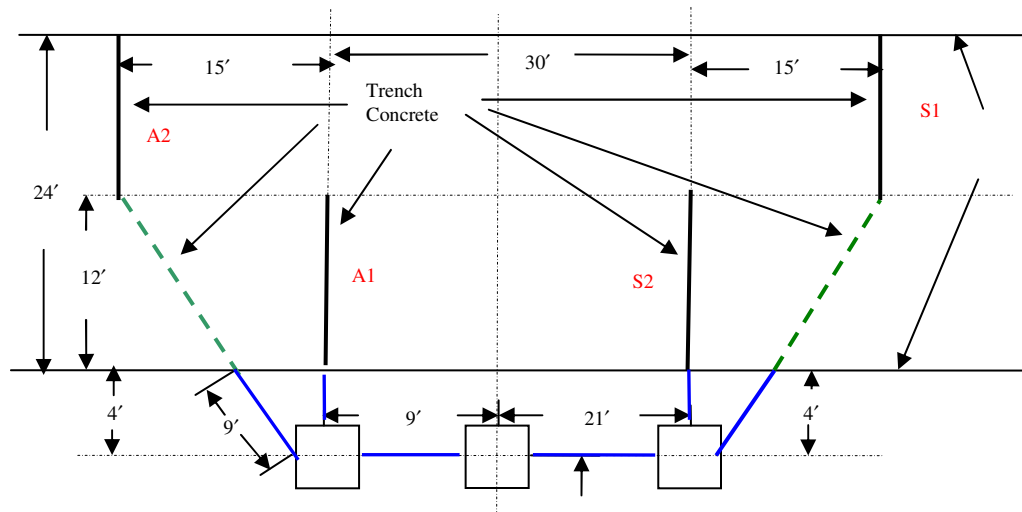


Fig. 31. WIM Riverside campus layout

In Fig. 31, S1 and S2 indicate slots for steel bar #1 and #2 respectively, and A1, A2 indicate slots for aluminum bar #1 and #2, respectively.

The procedure for installing the embedded metal bars with the sensors into road pavement is briefly depicted in Figs. 32 to Fig. 34. First, a concrete saw with a diamond impregnated blade was used to cut slots in the cement of the concrete road (Fig.32). The slots were cut perpendicular to the center line of the two lanes. In Fig. 31, the solid line indicates that the trench housing metal bar was cut with cross section of 1 inch \times 3.5 inches; the dashed lines indicate the slots used to house the extended fiber cables were cut with a cross section of 0.5 inches \times 3.5 inches. A hammer drill with a crystal bit was used to prepare saw cuts to ensure that the slots perfectly fit the metal bar, and then the saw cuts were vacuumed and cleaned with Toluene to allow for ideal bonding of the epoxy with road concrete. The metal bars were also cleaned with Toluene. Second, the

high performance epoxy adhesive was quickly mixed with the hardener and this mixed epoxy was rapidly poured into each slot at a ~0.5 inch depth. Even the surface, the final depth after filling is 3 inch to the surface. Third, the metal bar was put in the slot and the slot was filled with mixed epoxy up to the surface (Fig. 33), making the epoxy surface perfectly even with the road surface. Fourth, the fiber cable was housed into the slot and sealant was pumped in even with the road's surface. Fig. 34 shows the road with the embedded sensor bar after the epoxy and the sealant have dried.



Fig. 32. Sensor bar installation: Saw tooth cutting the slot in the road



Fig. 33. Sensor bar installation: putting the metal bar in the slot and filling it with epoxy up to the top



Fig. 34. Sensor bar installation: Final appearance after the epoxy and sealant have dried

6.4 Calibration of the FO-WIM Sensor Using the Falling Weight Deflectometer

The Dynatest Model 8002 FWD was used in the road test, it provides a practical way to evaluate the sensor performance. It is designed for multi-purpose pavement applications, and ideal for weigh-in-motion calibration. The impulse-type testing imparts a transient load onto the pavement surface, and the duration and magnitude of the force applied represents the load pulse induced by a truck moving at a moderate speeds. It can provide accurate information such as pressure, load profiles and deflection of the basin at different depths.

The FWD consists of sensors used to detect the height setting of the raised weights. The weights are raised by a hydraulic system, the weight is then free to fall via release from a catch. Force is applied to a hip plate through a rubber buffer, and then to a seating plate which interfaces with the road's surface. In between the hip plate and the seating plate, a load cell measures the load applied and several deflection sensors detect the deflection of the basin. The applied loads are controlled by the height of the weights are raised, not by adding weights.

A trailer mounted with the FWD was pulled to a position so that one center sensor was directly under the center of the seating plate (as shown in Fig. 35). Data were collected from three fiber sensors: the center sensor and the other two sensors to the right and left of the center sensor. Table 4 shows the sensor chosen and the position of the three sensors to one marked end of the bar. 7-9 levels of load were applied ranging from 5000-13000 pounds, with each level the increase in the load is around 1000 pounds. Each level consists of 20 similar applied loads for the study of repeatability. Two levels



Fig. 35 One marked steel bar sensor under the center of load disk of FWD

Table 4. Measured sensor number and position to the marked end of metal bar

	Center sensor	Left side sensor	Right side sensor
Steel bar	#3/ 39inch	#5/ 46inch	#2/ 32inch
Aluminum bar	#13/ 30inch	#15/ 46inch	#12/ 24inch

of unknown load tests were performed in order to study the ability of the sensors to predict unknown loads.

The signal from the steel bar sensors and the aluminum sensors are depicted in Fig. 36 and Fig. 37. All sensors showed clear and simultaneous pulse response to the main and residual impulses of applied loads. Figs. 38 and 39 demonstrate the repeatability of test results for the two bar sensors. It is evident that the sensors give very

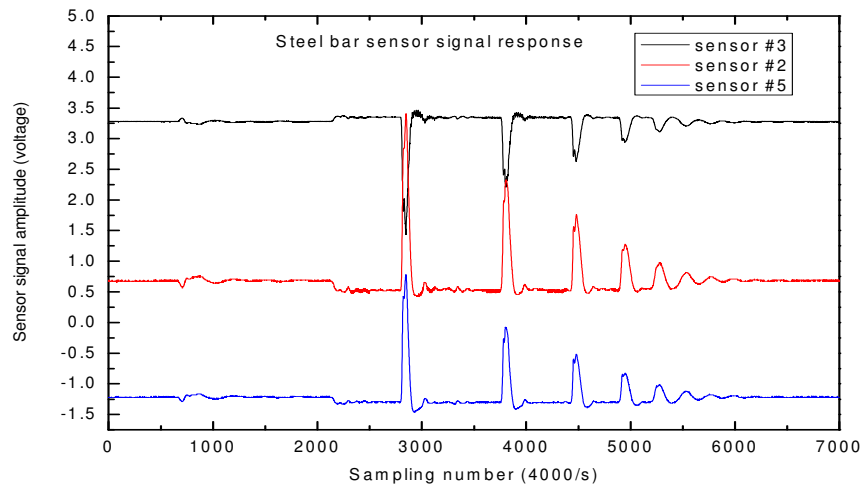


Fig. 36. Steel bar sensor responses to the FWD load applied at ~9000 pounds

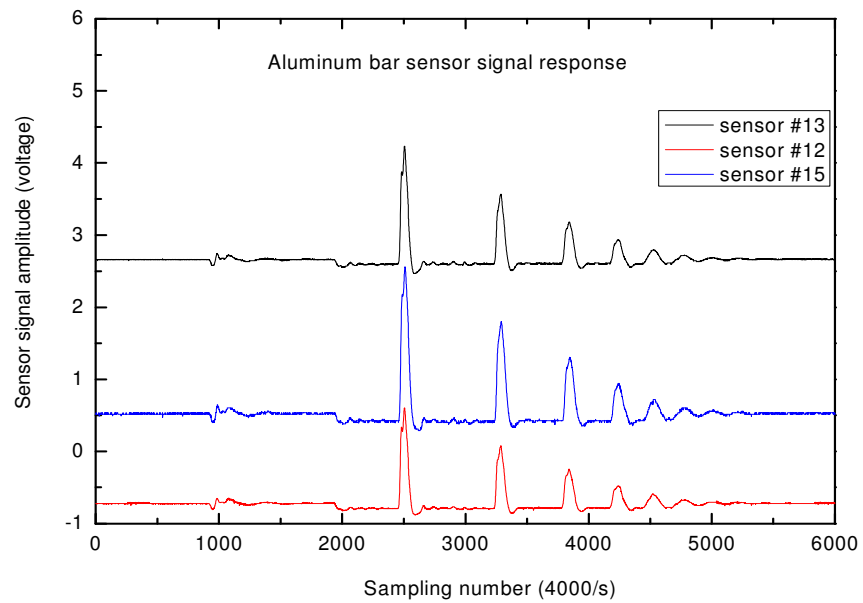


Fig. 37. Aluminum bar sensor responses to the FWD load applied at ~7600 pounds

stable signals with a standard deviation of less than 0.03 for the steel bar sensors and less than 0.05 for the aluminum bar sensors.

A closer look at the sensor output pulse shape in response to the real time profile of the FWD loads provided by the FWD system shown in Fig. 40. The traces of both aluminum bar sensors and steel bar sensors show good matches to the FWD load profiles, with the steel bar sensors offering closer match. The traces have been rescaled in the x and y axes to facilitate a comparison between them. The ripple in the FWD profile is induced by the rubber buffer which provides a buffering effect on the impact of the FWD.

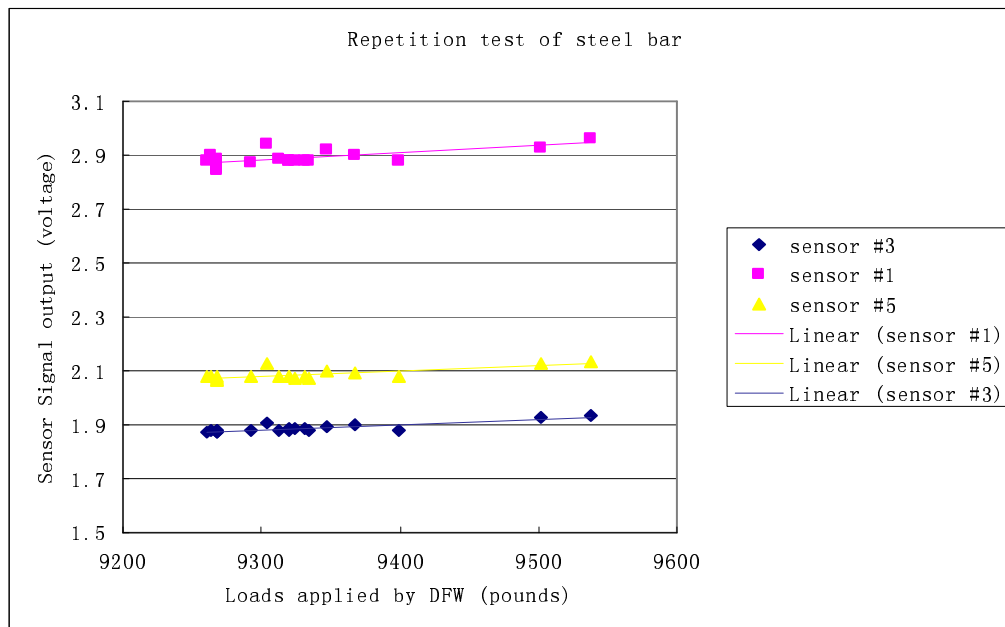


Fig. 38. Repeatability test of the steel bar sensors

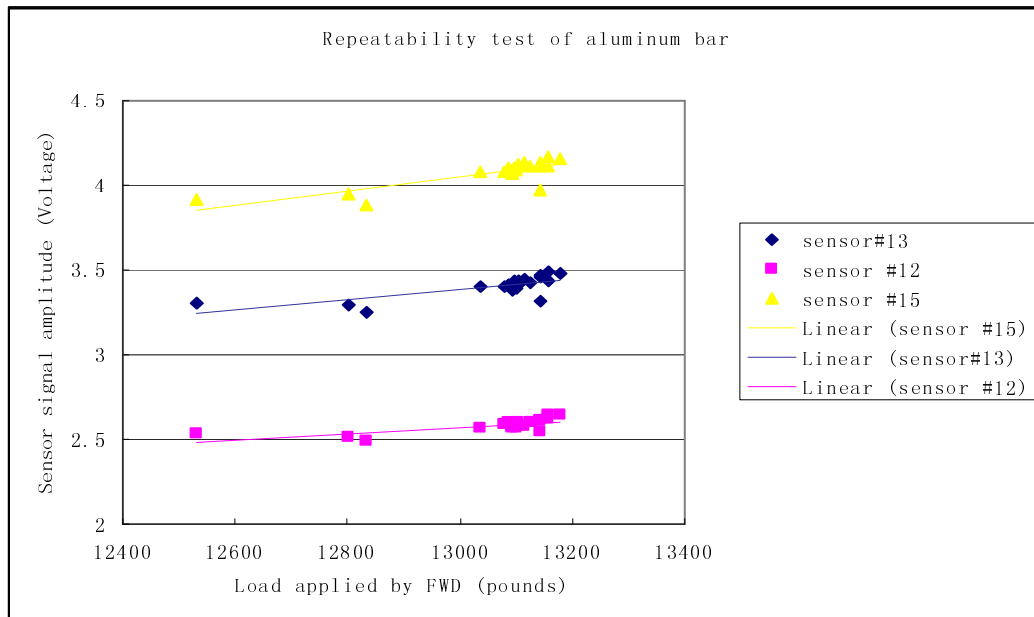


Fig. 39. Repeatability test of the aluminum bar sensors

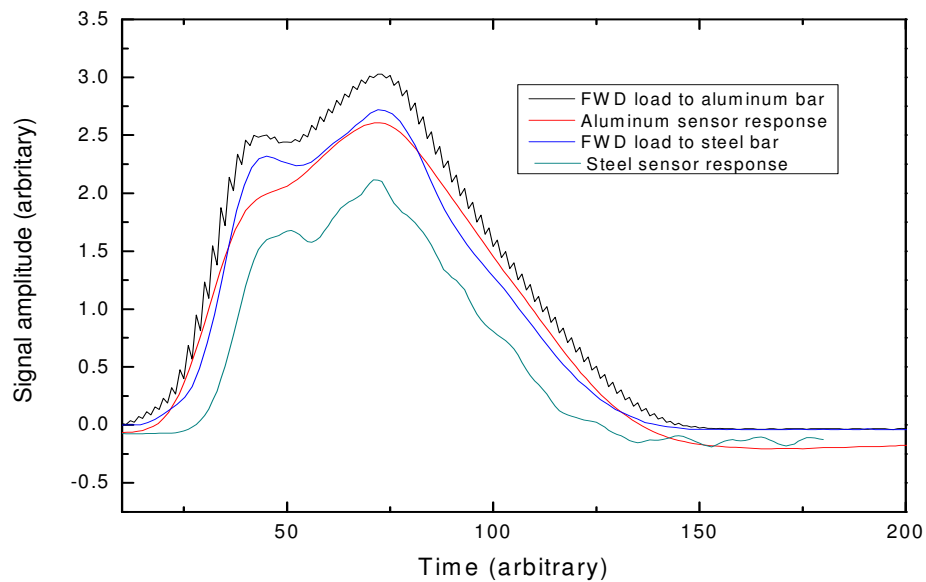


Fig. 40. Sensor responses to corresponding FWD load profiles

A series of tests were conducted to study the dependence of the sensor signal amplitude on the different levels of the FWD applied loads. Figs. 42 and 43 show the steel bar and aluminum bar sensor signal amplitudes variation versus several levels of FWD loads, respectively. Each level has 20 applications of similar loads. The y axis is the first peak amplitude and corresponds to the studied main load impact. The three lines are the least square linear regressions of the raw data, the dots. The linearity coefficient B (slope of the line) and interception V_0 of each sensor is shown in Tables 5 and 6. Figs. 42 and 43 clearly indicate that the sensor responses are highly linear; a coefficient of determination (COD) R^2 greater than 99.5% is achieved for all these sensors. The high degree of linearity of these sensor responses thereby indicates a high accuracy in correlating the sensor signal amplitude to the FWD applied loads. Thus a high accuracy can be expected in predicting unknown loads.

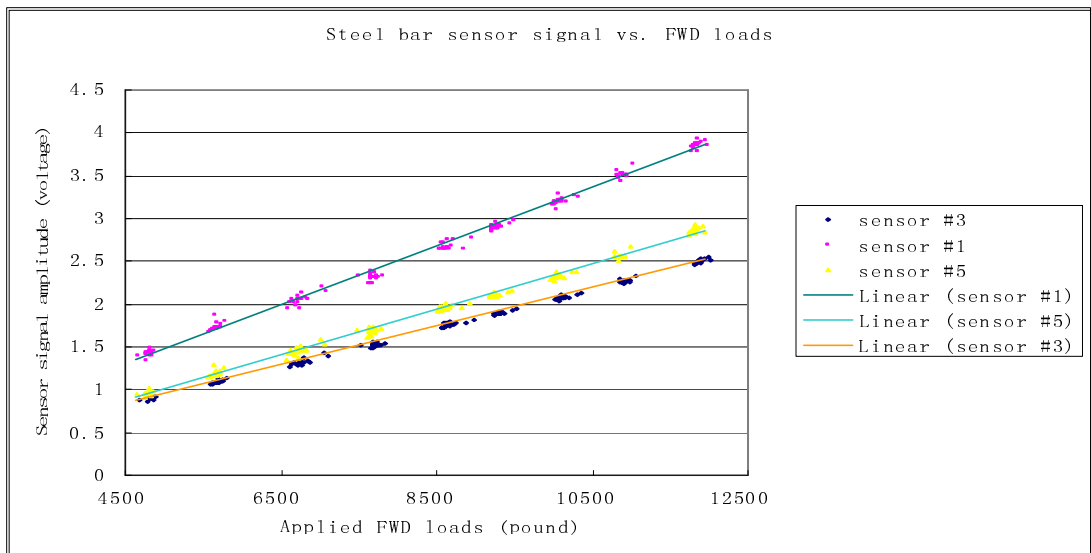


Fig. 41. Steel bar sensor responses to different FWD applied loads

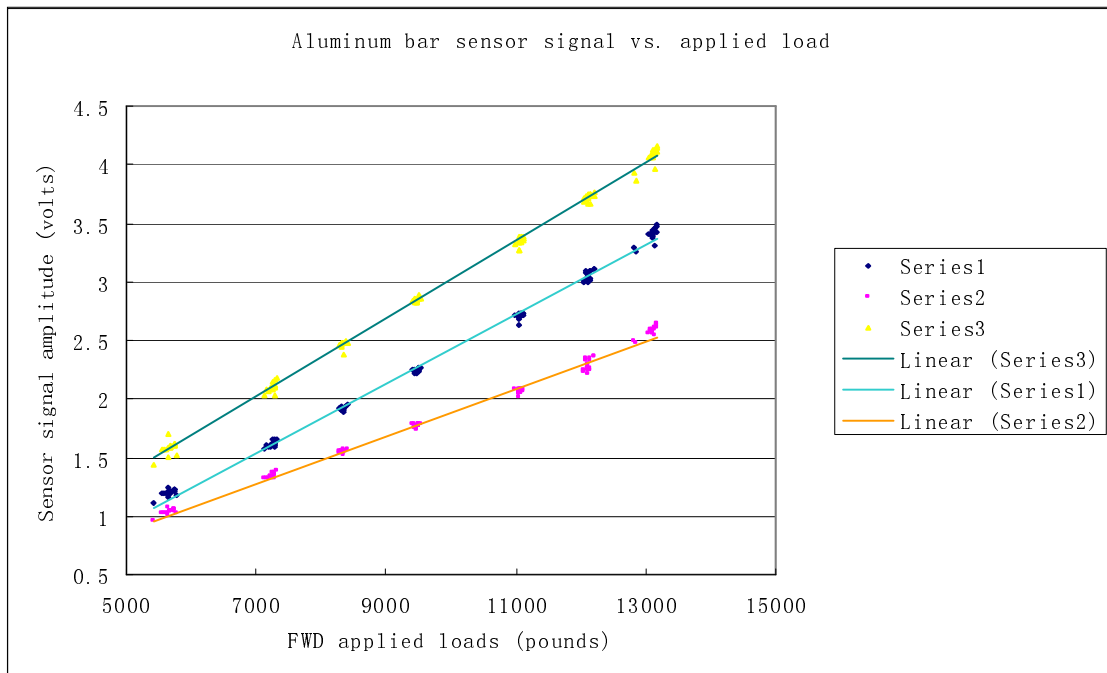


Fig. 42. Aluminum bar sensor responses to different FWD applied loads

Table 5. Linearity coefficients of steel bar sensors

	Sensor #3	Sensor #1	Sensor #5
B (voltage/pound)	$2.64 \cdot 10^{-4}$	$2.24 \cdot 10^{-4}$	$3.42 \cdot 10^{-4}$
V_0 (voltage)	-0.1959	-0.2680	-0.3511

Table 6. Linearity coefficients of aluminum bar sensors

	Sensor #3	Sensor #1	Sensor #5
B (voltage/pound)	0.000224	0.000342	0.000264
V_0 (voltage)	-0.195903	-0.268001	-0.351146

Two sets of each of the 20 unknown similar loads were tested in steel bar sensors. After obtaining the sensor signal amplitudes through data processing and by using the linearity coefficient in Table 5 we can get the predicted values that were applied FWD loads. The predicted values are then compared to the practical FWD load values later provided by TTI. The two sets are shown in Tables 7 and 8, respectively. A relative percentage error (RPE) was used to characterize the precision of the prediction.

$$RPE = \frac{load_{true} - load_{measured}}{load_{true}} \times 100\% . \quad (6.1)$$

Tables 7 and 8 clearly show the high accuracy the sensor achieved in estimating applied loads. The center sensor shows an extraordinary excellent prediction with regards to the unknown loads. The difference between the estimated value and the practical load value are all less than 5 pounds, and an RPE less than 0.05% is achieved. Another two sensors also showed an excellent prediction with an RPE less than 4.0% and 2.0% respectively. Using the average of the three sensor's estimation, the RPEs are less than 2.0%. The all negative RPEs are most likely induced by the minor laser instability and the thermal instability of the SCU system.

A wider range of unknown FWD loads were applied to the aluminum bar sensors, and the estimation results and RPEs are shown in Table 9. Compared to the steel bar sensors, the center sensor of the aluminum bar shows a higher RPE of less than 4%. The RPE of the other two sensors is less than 5% and 4%, respectively, which is generally higher than the steel bar sensors. However, after averaging the prediction of the three sensors, the average RPEs are all less than 2.0%.

Table 7. Prediction and RPE's of the steel bar FWD applied loads of data V series

V data series	sensor #3	sensor #2	sensor #5	real value	RPE #3	RPE #2	RPE #5	Avg. RPE
1	7502.889	7708.013	7645.641	7506.124	0.0431%	-2.6897%	-1.8587%	-1.5018%
2	7335.847	7565.914	7480.947	7339.216	0.0459%	-3.0889%	-1.9311%	-1.6580%
4	7353.327	7564.179	7496.559	7356.681	0.0456%	-2.8205%	-1.9014%	-1.5588%
5	7306.724	7562.013	7485.582	7310.116	0.0464%	-3.4459%	-2.4003%	-1.9333%
6	7323.965	7550.631	7440.181	7325.795	0.0250%	-3.0691%	-1.5614%	-1.5352%
7	7407.847	7614.096	7550.478	7411.158	0.0447%	-2.7383%	-1.8799%	-1.5245%
8	7375.001	7618.558	7495.802	7378.338	0.0452%	-3.2557%	-1.5920%	-1.6008%
9	7295.093	7471.081	7407.787	7298.495	0.0466%	-2.3647%	-1.4975%	-1.2718%
10	7343.617	7581.82	7464.677	7346.98	0.0458%	-3.1964%	-1.6020%	-1.5842%
11	7342.298	7571.371	7465.612	7345.661	0.0458%	-3.0727%	-1.6330%	-1.5533%
12	7299.591	7495.678	7410.005	7302.989	0.0465%	-2.6385%	-1.4654%	-1.3524%
13	7378.946	7572.179	7466.1	7382.28	0.0452%	-2.5724%	-1.1354%	-1.2209%
14	7319.986	7552.752	7427.713	7323.367	0.0462%	-3.1322%	-1.4248%	-1.5036%
15	7537.402	7776.408	7695.323	7540.609	0.0425%	-3.1271%	-2.0517%	-1.7121%
16	7300.228	7506.912	7407.734	7303.626	0.0465%	-2.7834%	-1.4254%	-1.3874%
17	7276.655	7512.749	7413.032	7280.071	0.0469%	-3.1961%	-1.8264%	-1.6585%
18	7354.98	7570.921	7462.127	7358.334	0.0456%	-2.8891%	-1.4106%	-1.4180%
19	7260.673	7444.807	7358.091	7264.103	0.0472%	-2.4876%	-1.2939%	-1.2448%
20	7493.768	7667.19	7575.433	7497.011	0.0433%	-2.2700%	-1.0460%	-1.0909%

Table 8. Prediction and RPE's of the steel bar FWD applied loads of data X series

X data series	sensor #3 prediction	sensor #2 prediction	sensor #5 prediction	real value	RPE #3	RPE #2	RPE #5	Avg. RPE
1	9859.736	9951.22	10013.07	9861.078	0.0136%	-0.9141%	-1.5413%	-0.8139%
2	9584.495	9675.07	9710.702	9586.059	0.0163%	-0.9285%	-1.3003%	-0.7375%
3	9654.707	9730.786	9772.234	9656.214	0.0156%	-0.7723%	-1.2015%	-0.6527%
4	9620.181	9706.189	9760.822	9621.715	0.0159%	-0.8780%	-1.4458%	-0.7693%
5	9566.169	9678.994	9693.739	9567.747	0.0165%	-1.1627%	-1.3168%	-0.8210%
6	9580.416	9712.539	9704.292	9581.983	0.0164%	-1.3625%	-1.2764%	-0.8742%
7	9712.776	9864.168	9896.513	9714.236	0.0150%	-1.5434%	-1.8764%	-1.1349%
8	9590.17	9705.695	9735.849	9591.729	0.0163%	-1.1882%	-1.5025%	-0.8915%
9	9549.969	9689.674	9713.105	9551.56	0.0167%	-1.4460%	-1.6913%	-1.0402%
10	9536.283	9651.544	9710.301	9537.885	0.0168%	-1.1917%	-1.8077%	-0.9942%
11	9586.684	9698.438	9736.095	9588.246	0.0163%	-1.1492%	-1.5420%	-0.8916%
12	9654.551	9839.744	9855.705	9656.058	0.0156%	-1.9023%	-2.0676%	-1.3181%
13	9386.141	9446.598	9487.878	9387.863	0.0183%	-0.6256%	-1.0654%	-0.5576%
14	9504.721	9651.397	9691.484	9506.348	0.0171%	-1.5258%	-1.9475%	-1.1521%
15	9517.203	9637.235	9665.853	9518.821	0.0170%	-1.2440%	-1.5446%	-0.9239%
16	9494.7	9616.503	9633.743	9496.335	0.0172%	-1.2654%	-1.4470%	-0.8984%
17	9527.555	9697.308	9715.28	9529.163	0.0169%	-1.7645%	-1.9531%	-1.2336%
18	9580.515	9666.66	9711.542	9582.081	0.0163%	-0.8827%	-1.3511%	-0.7391%
19	9631.883	9721.499	9736.67	9633.408	0.0158%	-0.9144%	-1.0719%	-0.6568%
20	9733.719	9855.202	9867.473	9735.163	0.0148%	-1.2330%	-1.3591%	-0.8591%

Table 9. Prediction and RPE's of the aluminum bar FWD applied loads

Data series	sensor 13 prediction load	sensor 12 prediction load	sensor 15 prediction load	real force	RPE #13	RPE #12	RPE #15	Avg. RPE
h01	10579.36	10799.78	10580.15	10805	2.09%	0.05%	2.08%	1.41%
h04	10471.97	10538.24	10468.13	10813	3.15%	2.54%	3.19%	2.96%
h06	6635.078	6584.071	6506.253	6662	0.40%	1.17%	2.34%	1.30%
h07	10484.6	10640.81	10516.47	10869	3.54%	2.10%	3.24%	2.96%
h12	10268.22	10393.96	10181.31	10686	3.91%	2.73%	4.72%	3.79%
h13	10526.22	10740.77	10685.51	10801	2.54%	0.56%	1.07%	1.39%
h14	10479.86	10584.8	10521.27	10809	3.05%	2.07%	2.66%	2.59%
h15	10491.13	10634.03	10492.3	10785	2.72%	1.40%	2.71%	2.28%
h16	6622.66	6492.865	6623.952	6630	0.11%	2.07%	0.09%	0.76%
h18	10443.37	10561.36	10572.83	10770	3.03%	1.94%	1.83%	2.27%
h19	10660.47	10766.75	10906.58	10853	1.77%	0.79%	-0.49%	0.69%
k02	6814.19	6877.65	6787.136	6718	-1.43%	-2.38%	-1.03%	-1.61%
k04	6754.196	6763.344	6694.686	6674	-1.20%	-1.34%	-0.31%	-0.95%
k07	6729.616	6663.375	6655.956	6630	-1.50%	-0.50%	-0.39%	-0.80%
k08	6754.519	6733.195	6650.935	6666	-1.33%	-1.01%	0.23%	-0.70%
k10	6651.601	6496.911	6628.85	6582	-1.06%	1.29%	-0.71%	-0.16%
k12	6563.252	6445.063	6423.189	6630	1.01%	2.79%	3.12%	2.31%
k14	6677.555	6590.052	6650.412	6630	-0.72%	0.60%	-0.31%	-0.14%
k15	6659.578	6550.665	6664.771	6590	-1.06%	0.60%	-1.13%	-0.53%
k17	6594.847	6485.709	6590.123	6543	-0.79%	0.88%	-0.72%	-0.21%
k20	6490.44	6321.107	6347.716	6575	1.29%	3.86%	3.46%	2.87%

6.5 Evaluation of Sensor Performance under Varying FWD Load Positions

An evaluation of sensor performance under varying FWD loads positions was also performed. Around 10 positions along the line of the bar were chosen; in each position, 3 levels of loads around 6500, 10000, and 13000 pounds were applied, each level includes 5 similar load applications. Figs. 43 and 44 show examples of steel and aluminum bar sensor responses with varying load positions, respectively. The peak amplitudes under the three specific loads were obtained through linear regression of the 3 levels of data retrieved from each position, and the distance is measured from the sensor position to the center of the circular seating plate.

A nonlinear, symmetric, bell shaped distribution of the sensor signal's amplitude as it varied with each load position is displayed here. The maximum is reached at around the 0 inch position, which is quite reasonable; Fig. 44 also shows that one point near the 0 inch position has the same amplitude with the 0 inch's. In about 10 inches of displacement, the signal's amplitude decreases over 3dB. At around 30 inches of displacement the signal almost drops to zero. Our experimental results were then compared to the BISAR simulation, a multilayer linear elastic program developed by the Shell Company. BISAR is widely used in layered elastic road performance analysis; it facilitates the mechanistic modeling of the pavement structure and calculates the stresses and strains caused by vehicle loading. In our simulation, a typical pavement structure was modeled as a multi-layered elastic system, with circular uniform loads of a radius of 5.9 inches with only a vertical stress, in order to simulate the FWD loads.

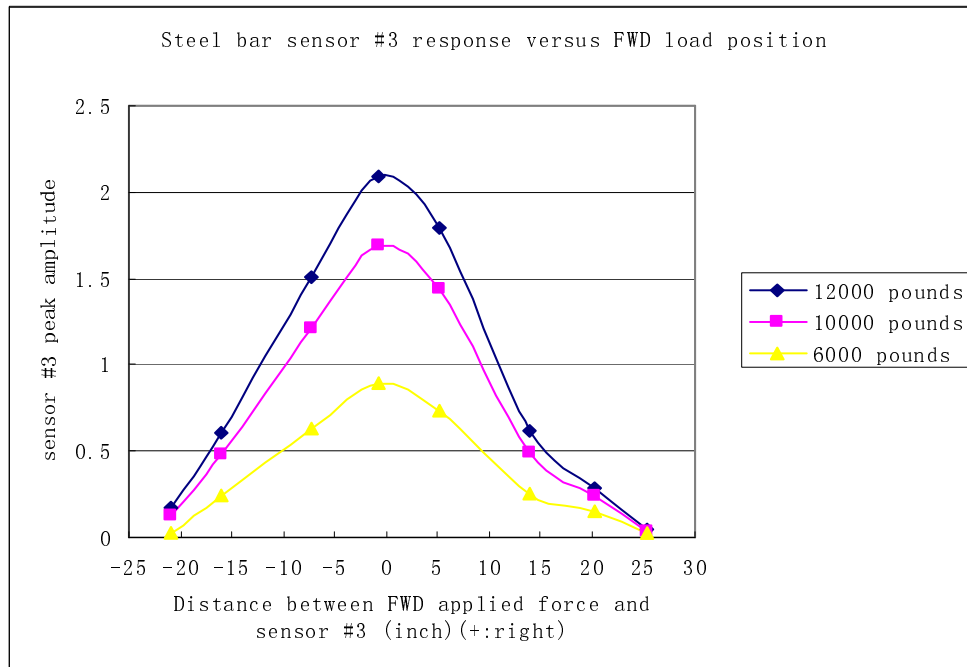


Fig. 43. Variation of steel bar sensor #3 responses with the FWD load position

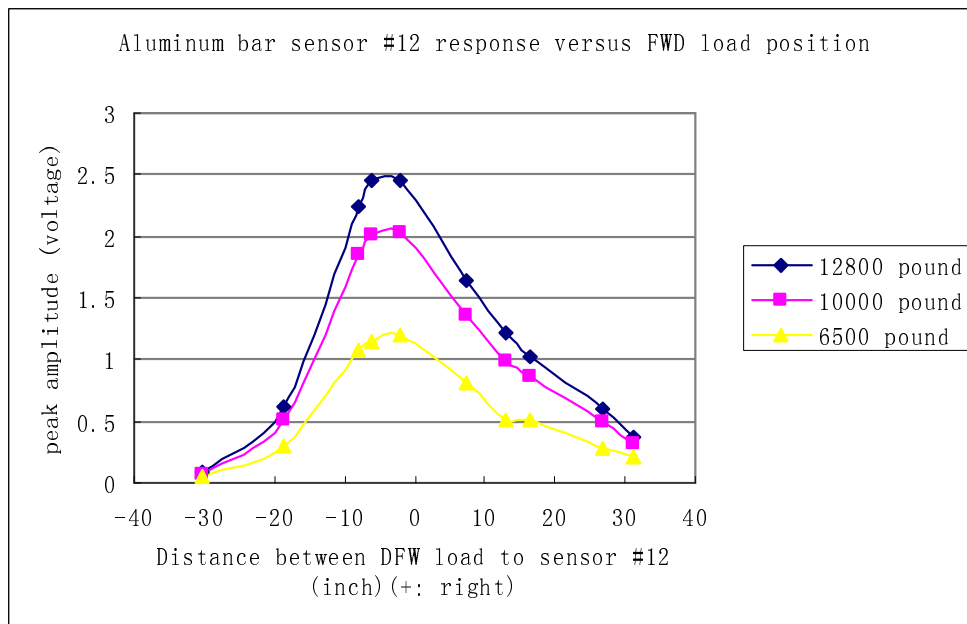


Fig. 44. Variation of aluminum bar sensor #12 responses with the FWD load position

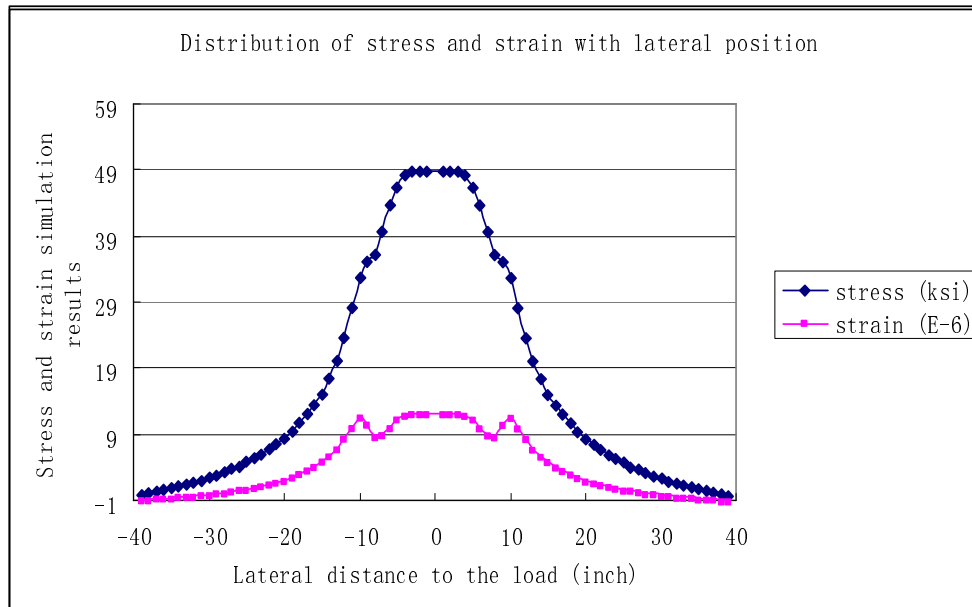


Fig. 45. BISAR simulation results of stress and strain variations with the load position

The BISAR results are shown in Fig. 45. It is evident that our results are in agreement with the simulation results, which show that the strain has a good bell-shaped distribution. As expected there are discontinuity problems at the edge of the circular load, but this couldn't be shown in our test due to the limited test spots.

This position distribution of sensor responses suggests an optimized sensor network distribution which would need to be figured out for real road applications of this sensor.

6.6 Sensor Performance in Truck Tests and Analysis

Truck tests were performed in the test area. The two-wheel truck has two front tires and four rear tires. The related parameters of the truck are listed in Table 10. The two numbers on the rear tires indicate the outside/inside value.

Table 10. Parameters of the truck

		Weight (pound)	Tire width (inch)	Lateral distance (inch)	Tire pressure (Lbs)
Front	Left	4980	8.5	90	74
	Right	4900	7.5		72
Rear	Left	6480	9/7.5	94.5	78/80
	Right	7380	8/7.5		82/70

The truck was driven at speeds of 25-40 miles per hour, from north to south, along the center of the two lanes. Totally four channel signals were collected: two sensors from S_1 and S_2 , respectively, or two sensors from A_1 and A_2 , respectively.

Figs. 46 and 47 shows the signal collected from the steel bar sensor and the aluminum bar sensor, respectively, after initializing the baseline to zero. Because S_1 and S_2 , A_1 and A_2 have a longitudinal distance, the two figures show two groups of wheel passing clearly. This allows us to measurement the truck speed, along with the clear front and rear wheel peak separation, which in turn allow us to get a good measurement of the axel distance.

Both Figs. 46 and 47 didn't show a constant ratio of the signal amplitude of the rear wheel to front wheel due to the front tire and rear tire being in different lateral positions. We also can observe the fact that some aluminum bar sensors show a ripple in top of the pulse, which happens more often than in the steel bar sensors through the

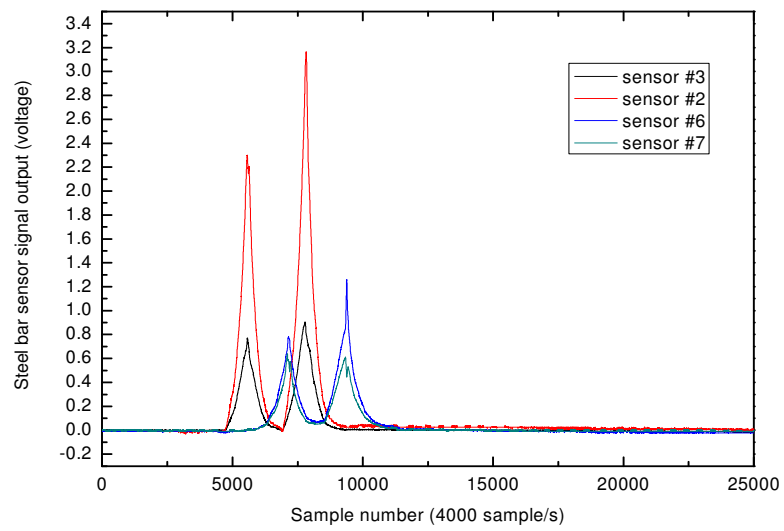


Fig. 46. Steel bar sensor responses to truck wheel crossings

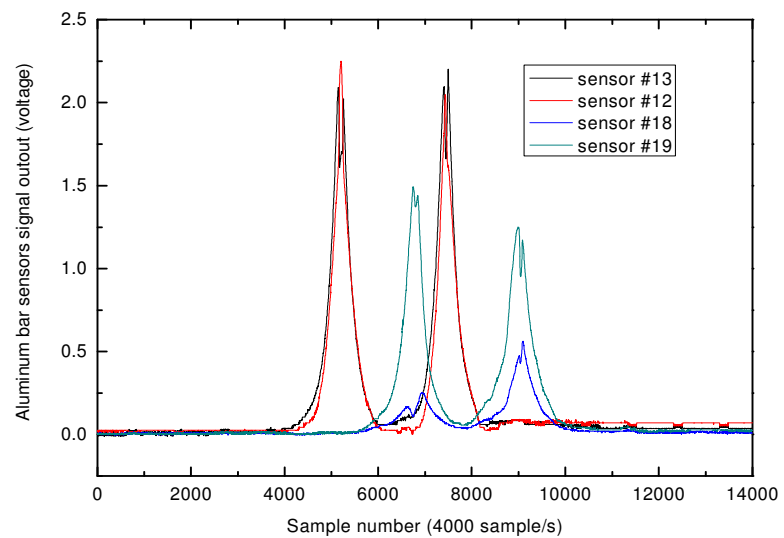


Fig. 47. Aluminum bar sensor responses to truck wheel crossing

entirety of the tests. The possible reason is that aluminum is more sensitive to the road's unevenness.

To closely study the sensor's response to the truck wheels in the passing position, lime powder was used to record the trace of the rear right outside tire. Approximately 40 tests were conducted for the steel bar and the aluminum bar sensor, respectively, and 4 or 5 tests with each truck wheel passing at similar positions were performed to study the repeatability of the sensor's response.

Figs. 48 and 49 show the good repeatability of the sensors responses to similar truck crossing positions. The signal amplitude is almost the same for both the aluminum bar sensors and the steel bar sensors. The different position of the first peak is due to the truck passing at a slightly different speed. The three clearly identified front wheel peaks only have a time separation of $1/8$ of a second. This indicates that our sensor can precisely measure speed of truck.

Fig. 50 shows the sensor #3 output amplitudes in response to different wheels passing positions. Around one location, the first wheel had one maximum amplitude whereas the second peak shows that in two locations it reaches maximum amplitude, separating around 20 inches, which is exactly the two tires' distance in the rear right. However, generally speaking, the distributions are not as good as we obtained from the FWD test. Fig 51 shows the aluminum bar sensor's response to different wheels passing position. The result is not good at all, it didn't show a very stable distribution for the aluminum bar sensors when the truck passed in different positions.

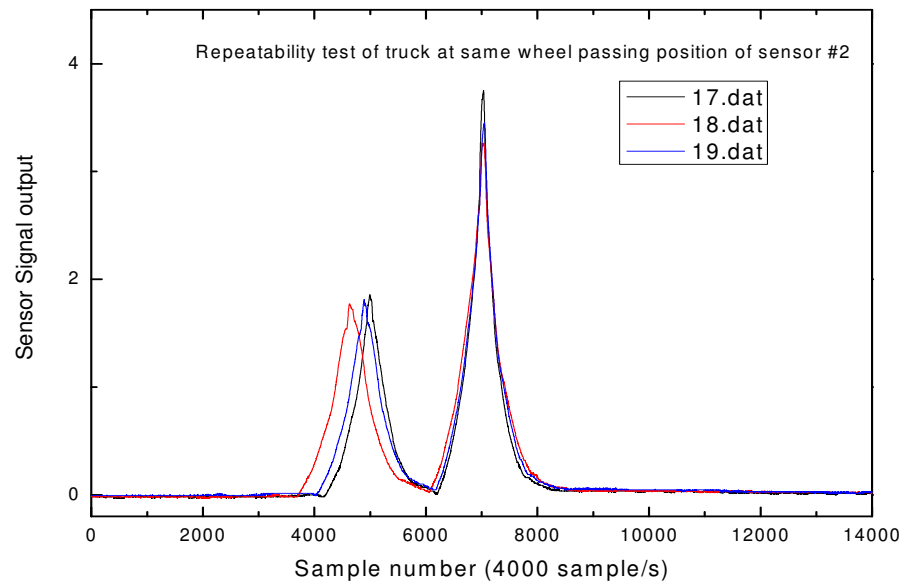
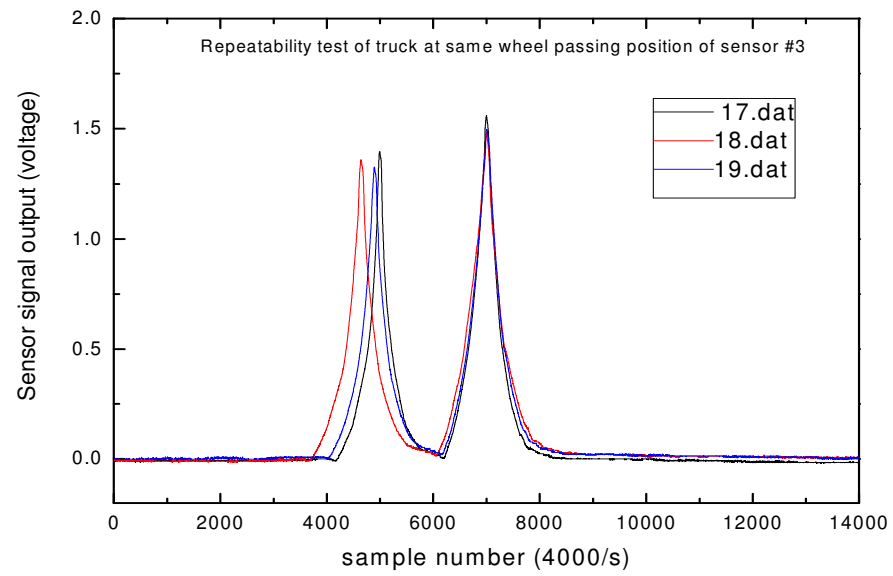


Fig. 48. Repeatability: two steel bar sensor responses to truck wheel crossings at the same position

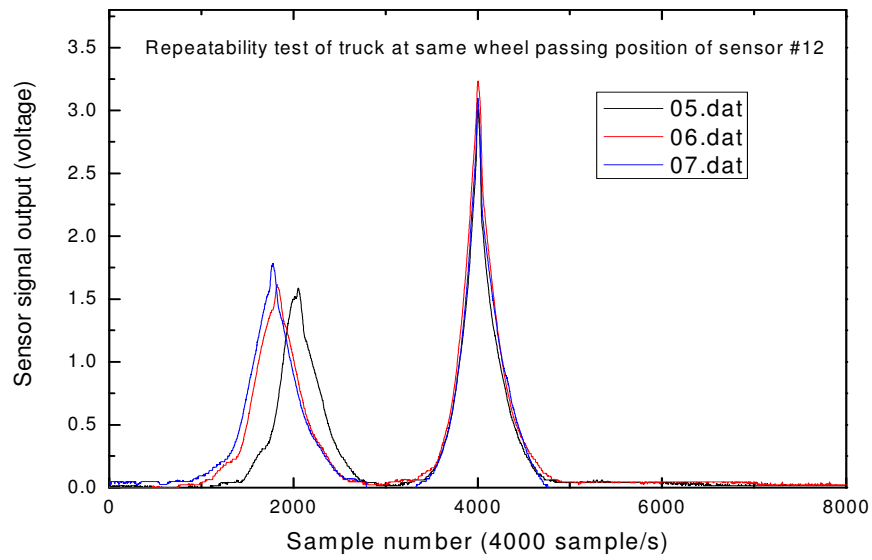
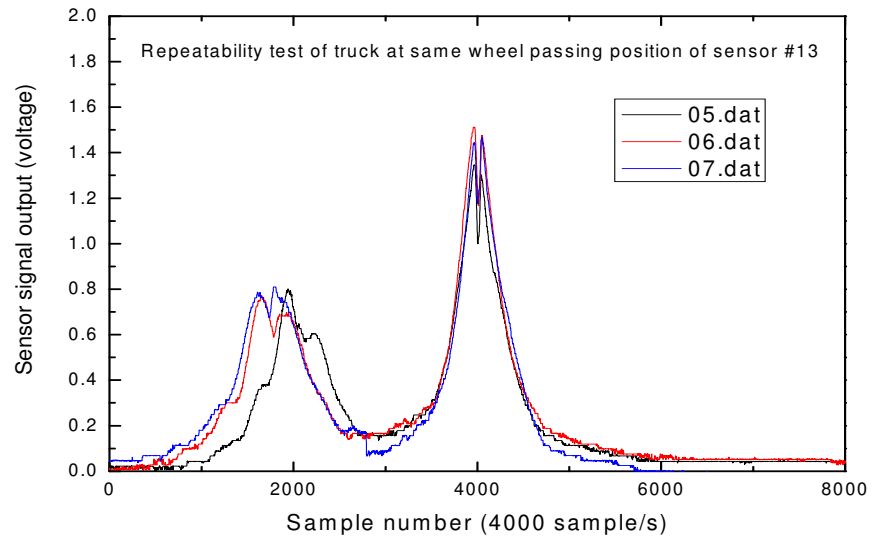


Fig. 49. Repeatability: two aluminum bar sensor responses to truck wheel crossing at the same position

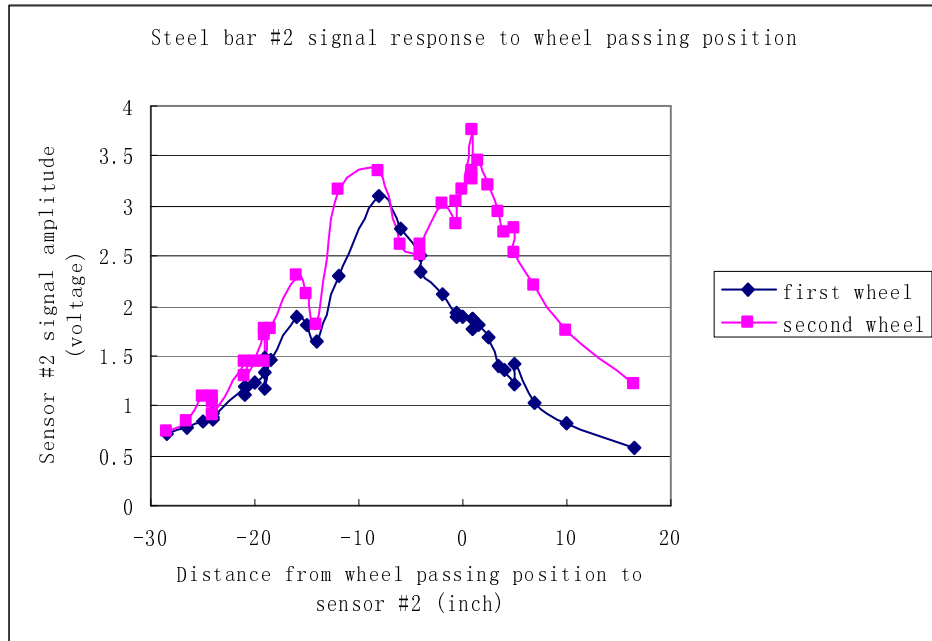


Fig. 50. Steel bar sensor #3 output amplitude variation with FWD load positions

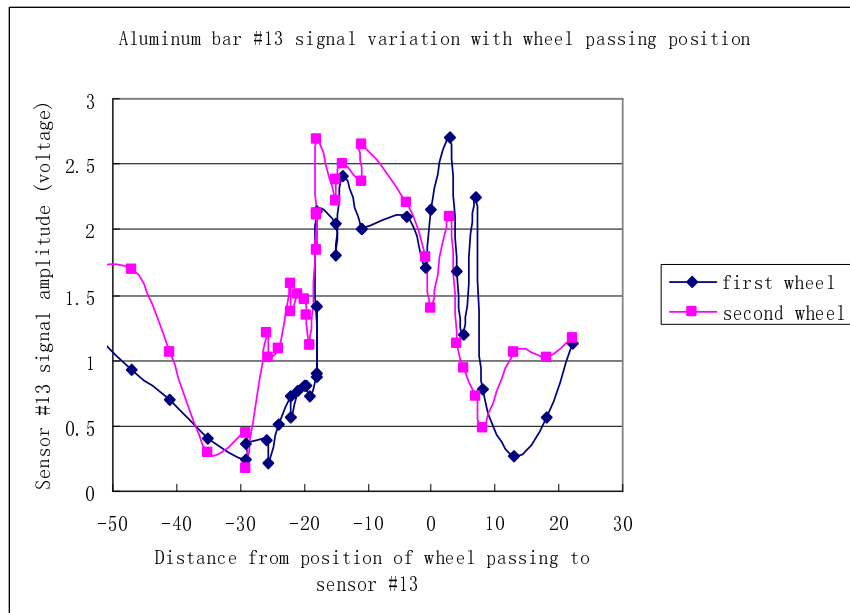


Fig. 51. Aluminum bar sensor #13 output amplitude variation with FWD load positions

The general inefficiency of the sensor performance in the real truck tests is attributable to the complexity of the impact the tire applied to the ground as compared to the FWD's. The force is involved in three directions: x, y and z, instead of only in the z direction. Thus the induced stress includes vertical, lateral and transverse stresses, and will also be affected by different tire types which will induce different stress distributions [33][34]. The aluminum bar sensors are further influenced by the low material stiffness.

CHAPTER VII

CONCLUSIONS

Research on two practical applications of the FFPI sensor was successfully conducted.

An optical binary switch for airplane applications based on white light interferometry has been demonstrated. The strain measured by the sensing element shows excellent linearity as a function of the force applied; good agreement between calculated and experimental results was observed. By properly setting a threshold, the system produces a binary signal indicating the state of the pilot-actuated system; i. e., whether or not the button is being pushed.

Research in fiber-optic weigh-in-motion sensors show that the FFPI sensor has a great potential for measuring the truck axel and gross weight. An important achievement is that the steel bar center sensor can now estimate the FWD load with extraordinary precision. In all test data, the predicted value is shown to be less than 5 pounds of difference from the practical value (upon 9000 pounds) later provided by TTI. The experiments show that the two sensor assemblies both have the ability to predict vertical loads with an average RPE less than 2%. The sensor signals matches very well to the time profiles of the FWD loads. The FFPI sensors also demonstrate their ability to measure axel distance, truck speed, and truck type. An evaluation of sensor performance under varying load positions shows that the sensor's behavior agrees with BISAR simulations in the FWD test, and a bell shaped distribution is observed. In the truck test,

the sensor showed a good level of repeatability with similar wheel crossing positions. In all of the tests, the steel bar sensors performed better than the aluminum bar sensors. The inefficiency of the sensor performance in weighing the trucks originates mainly from its signal dependency on position. The complexity of tire impact induced stress is also important. These two problems can be overcome by first: redesigning the metal bar structure and the surrounding material to eliminate the shear stress; secondly by optimizing distribution the sensor network along a lane; and third by minimizing the lane width in the test spot.

We can conclude that the proposed fiber FFPI weigh-in motion sensor has a great potential to be a long-lasting, cost-effective solution for truck classification and WIM applications.

CHAPTER VIII

RECOMMENDATIONS

Concerning the binary optical switch, future tests should be done to test the system performance at different temperatures. The reference and sensing sensor should experience the same temperature. The whole setup is now on an optical table, integrating the optical system into one box with vibration protection is suggested for real airplane applications, and the ability of the system to handle vibrations needs to be studied. The ability to extend one sensing sensor to the multiplexing of many sensors on a single fiber is promising. Thus, in one optical system, multiple binary switches can be realized. To achieve better results, the mirror reflectance of the FFPI needs to be optimized. Also, a new configuration of connecting multiple sensors through couplers needs to be figured out to efficiently utilize the SLD light source.

In sensor fabrication, new techniques will be needed to overcome the brittleness of the sensor. A recoating of plastic buffer is necessary to protect the sensor from being broken, especially when the sensor functions as a strain sensor.

The results of the fiber-optic weigh-in-motion sensors have shown the feasibility of using FFPI sensors in monitoring heavy traffic. FFPI sensors have proved to have the ability of precisely measure the vertical load, axle spacing, traffic speed, and truck class. In addition steel bar sensor's performance is better than that of the aluminum bar. The sensors performance in axel weight and gross weight is influenced by the position of the wheel crossing and shear stresses. It will be necessary to modify the design of the metal bar and the embedding process. More elastic and long-lasting material should be chosen

to surrounding the bar, well on the top and on the bottom using the same epoxy. This may help buffer the shear stress.

A sensor network of non-even sensor distribution is suggested, according to the Gaussian distribution of truck wheels passing in a highway across lane. Sensors should mainly be embedded in the two sides of the lane, with separation of 5-6 inches, avoiding the middle area and the very end of the lane where there is little chance of wheel crossing. The suggested sensor distribution is shown in Fig. 52. It's obvious that the more sensors there are, the better performance that can be expected.

Finally, the sensor's performance needs to be monitored under actual traffic conditions. Other aspects such as integrating into existing weigh-in-motion monitoring and classification systems to compare the performance should also be undertaken.

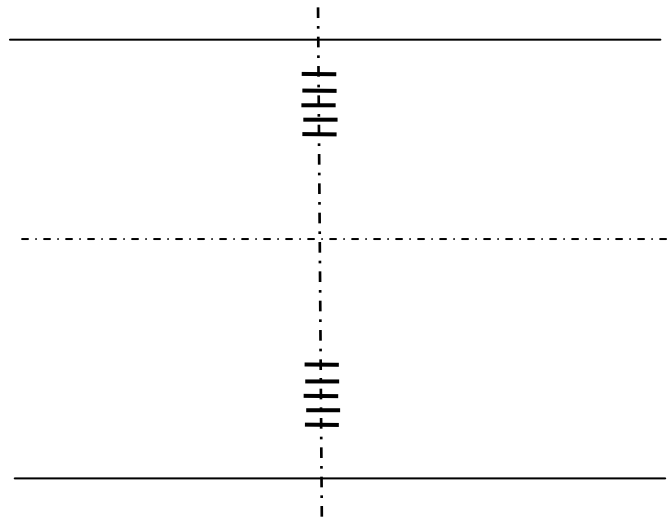


Fig. 52. Suggested sensor distribution across a lane

REFERENCES

- [1]. K. Wood, T. Brown, R. Rogowski and B. Jensen, "Fiber optic sensors for health monitoring of morphing airframes: I. Bragg grating strain and temperature sensor," *Smart Mater. Struct.*, vol. 9, pp. 163-169, Apr. 2000.
- [2]. Z. Xie, H. F. Taylor, "A fiber optic binary switch for aircraft application," in *Proc. IEEE Sarnoff Symposium*, Princeton, New Jersey, Mar. 2006.
- [3] P. J. Cosentino, W. Eckroth, B. G. Grossman, " Analysis of fiber optic traffic sensors in flexible pavements," *J. of Transp. Eng.*, vol. 129, no 5, pp. 549-547, Sep. 2003.
- [4] C. I. Merzbacher, A. D. Kersey and E. J. Friebele, "Fiber optic sensors in concrete structures: a review," *Smart Mater. Struct.*, vol. 5, pp 196-208, Apr.1996.
- [5] M. Quirion and G. Ballivy, "Concrete strain monitoring with Fabry-Perot fiber-optic sensor," *J. Mat. Civ. Eng.* vol. 12, pp. 254-260, Nov. 2000.
- [6] S. R. Teral, "Fiber optic weigh in motion: looking back and ahead," in *Proc. SPIE*, vol. 3326, pp 129-137, Jun., 1998.
- [7] W. L. Schulz, E. Udd, J.M. Seim, G. E. McGill, "Advanced fiber-grating strain sensor systems for bridges, structures and highways," in *Proc SPIE*, vol. 3325, pp. 212-223, Jun. 1998.
- [8]. C. E. Lee and H. F. Taylor, "Interferometric optical fibre sensors using internal mirrors," *Electron. Lett.*, vol. 24, pp. 193-194, Feb. 1988.
- [9] C. E. Lee, R.A. Atkins, and H. F. Taylor, "Performance of a fiber-optic temperature sensor from -200 to 1050°C," *Opt. Lett.*, vol. 13, no. 11, pp. 1038-1040, Nov. 1988.

- [10] Y. Yeh, C. E. Lee, R.A. Atkins, W. N. Gibler, and H. F. Taylor, "Fiber optic sensor for substrate temperature monitoring," *J. Vac. Sci. Technol.*, vol. 8, no. 4, pp. 3247-3250, Jul. 1990.
- [11] C. E. Lee, J. J. Alcoz, Y. Yeh, W. N. Gibler, R.A. Atkins, and H. F. Taylor, "Optical fiber Fabry-Perot sensors for smart structures," *Smart Mater. Struct.*, vol. 1, pp. 123-127, Jun. 1992.
- [12] C. E. Lee and H. F. Taylor, "Fiber-optic Fabry-Perot temperature sensor using a low-coherent light source," *J. Lightwave Technol.*, vol. 9, no. 1, pp. 129-134, Jan. 1991.
- [13] Y. Yeh, "Development of fiber-optic interferometric temperature sensor system," Ph.D. dissertation, Dept. Elect. Eng., Texas A&M Univ., College Station, 1991.
- [14] J. H. Lee, "A novel signal processing algorithm for FFPI and its sensor system application," Ph.D. dissertation, Dept. Elect. Eng., Texas A&M Univ., College Station, 1994.
- [15] M. C. Wang, "Fiber-optic Fabry-Perot sensor system using a low-coherent LED light source," Ph.D. dissertation, Dept. Elect. Eng., Texas A&M Univ., College Station, 1995.
- [16] R. Sadkowski, C. E. Lee, and H. F. Taylor, "Multiplexed interferometric fiber optic sensors with digital signal processing," *Appl. Opt.*, vol. 34, no. 25, pp. 5861-5866, Sep. 1995.
- [17] T.W. Kao and H. F. Taylor, "High-sensitivity intrinsic fiber-optic Fabry-Perot pressure sensor," *Opt. Lett.*, vol. 21, no. 8, pp. 615-617, Apr. 1996,.

- [18] Y. Park, "Development and testing of fiber optic current transducer with digital signal processing," Ph.D. dissertation, Dept. Elect. Eng., Texas A&M Univ., College Station, 1995.
- [19] R. Sadkowski, "Mixed-signal processor for a Fabry-Perot interferometric fiber optic pressure sensor," Ph.D. dissertation, Dept. Elect. Eng., Texas A&M Univ., College Station, 1994.
- [20] T. Bae, "Spark-plug mounted fiber optic sensor for measuring in-cylinder pressure in engines," M.S. Thesis, Dept. Elect. Eng., Texas A&M Univ., College Station, 2001.
- [21] W. Lee, "Railroad bridge monitoring systems with fiber optic sensors," Ph.D. dissertation, Dept. Elect. Eng., Texas A&M Univ., College Station, 1998.
- [22] H. S. Chio, H. F. Taylor and C. E. Lee, "High performance fiber-optic temperature sensor using low-coherence interferometry," *Opt. Lett.*, vol. 22, no. 23, pp. 1814-1816, Dec. 1997.
- [23] S. Chen, A. W. Palmer, K. T. V. Grattan and B. T. Meggit, "Digital signal processing techniques for electronically scanned optical fiber white light interferometry," *Appl. Opt.*, vol. 31, no. 28, pp. 6003-6010, Oct. 1992.
- [24] Y. J. Rao, Y. N., Ying and D. A. Jackson, "Compounded source for white light interferometry systems," in *Proc. 9th Optical Fiber Sensor Conference*, Firenze, Italy, pp. 275-278, Oct. 1993.
- [25] V. Bhatia, M. J. De Vries, K. A. Murphy and R. O. Claus, "Extrinsic Fabry-Perot interferometers for absolute measurement," *Fiber Optic Products News*, pp. 9-10, Dec. 1994.

- [26] T. Li, A. Wang, K. Murphy, and R. Claus, "White-light scanning fiber Michelson interferometer for absolute measurement," *Opt. Lett.*, vol. 20, no. 7, pp. 785-787, Apr. 1985.
- [27] H. Jinag, "Analysis and application for fiber-optic Fabry-Perot sensors using a low coherence length light source," Ph.D. Dissertation, Dept. Elect. Eng., Texas A&M Univ., College Station, 1996.
- [28] H. S. Choi, "Fiber optic Fabry-Perot temperature sensor system based on low coherence interferometer", Ph.D. Dissertation, Dept. Elect. Eng., Texas A&M Univ., College Station, August 1997.
- [29] Y. Chen and H. F. Taylor, "Multiplexed fiber Fabry-Perot temperature sensor system using white light interferometry," *Opt. Lett.*, vol. 27, pp. 903-905, Jun. 2002.
- [30] H. Nagai, Y. Noguchi, and S. Sudo, "High power high efficiency 1.3 μ m superluminescent diode with a buried bent absorption guide structure," *Appl. Phys. Lett.*, vol. 54, no. 18, pp. 1719-1721, May. 1989.
- [31] Y. Kashima, A. Matoba and H. Takano, "Performance and reliability of InGaAsP superluminescent diode," *J. Lightwave Tech.*, vol. 10, no 11, pp. 1644-1649, Nov. 1992.
- [32] S.T. Dai, D. V. Deussen, M. Beer, D. Rettner, G. Cochran, "Investigation of flexible pavement response to truck speed and FWD load through instrumented pavements," in *Proc., 8th Int. Conf. on Asphalt Pavements*, vol. I, pp 141–158, 1997.
- [33] R. V. Siddharthan, N. Krishnamenon, M. El-Mously, and P. E. Sebaaly, "Investigation of tire contact stress distributions on pavement response," *J. Transp. Eng.*, vol. 128, no. 2, pp. 136-144, Mar. 2002.

APPENDIX

PROGRAM LIST

```

/*****/
/* This program is designed for signal processing of WLI interferometer, the
detailed algorithm is explained in Chapter IV:
    1. Filter: 5 points average
    2. Normalization
    3. Correction of SLD data from DFB data
    4. Peak finding: hypothesis test
    5. Fine tune resolution enhancement
Compiler: Microsoft Visual C++6.0
Final revised on Oct. 4, 2004 by Zhaoxia Xie
*/
/*****/
#include<math.h>
#include<stdlib.h>
#include<stdio.h>
#include<iomanip.h>

#define DFB a

const int R=3000;          // ref and sen peaks are in range of -R to +R
const int np=50;          // np:# of points in one period of DFB
const int ng=2500;
//const int K=40;
const int t=1;           // used in find hcp
const int T=40;
const int R1=2,R2=4,R3=6;

const int Max_samples=15000;
const int Num=1500;
const int Q=70;          //hpdat[Q][P] need adjusting
const int P=19;
const int Z=40;          //used in calculate:pcorr_sum
const int F=500;          //used in correlation with cosine curve
int i,M,N,k,m,K;          //M:Total readin data number, N: useful data
float d,b,y,dxa,dxb;
FILE *fp,*fpc,*fp1,*fp2,*fp3;

char filename[30];
char temp[12];

```

```

int main(int argc, char *argv[])
{float SLD_sen_in[30000],SLD_ref_in[30000],DFB_in[30000];
  float SLD_sen[Max_samples],SLD_ref[Max_samples],DFB[Max_samples];
  if((fp=fopen(argv[1],"r"))==NULL)
  {fprintf(stderr,"Error opening original file.\n");
  exit(1);
  }
  while(!feof(fp))
  {
  fscanf(fp,"%f %f %f\n", SLD_ref_in+i,SLD_sen_in+i,DFB_in+i);
    i++;
  }
  M=i+1;          // M is the total readin sample points
  If (M>30000)
  {printf("Something wrong,M>30000\n");
  exit(0);
  }
  printf("TOTAL sample points is:M=%d\t",M);
  fclose(fp);
  /*****          cut data          *****/
  int index_ref=0;
  int index_sen=0;
  int index1,index2;
  float max_SLD_ref=SLD_ref_in[0];
  float max_SLD_sen=SLD_sen_in[0];
  for(i=1;i<M;i++)
  {if(max_SLD_ref<=SLD_ref_in[i])
  {max_SLD_ref=SLD_ref_in[i];
  index_ref=i;
  }
  if(max_SLD_sen<=SLD_sen_in[i])
  {max_SLD_sen=SLD_sen_in[i];
  index_sen=i;
  }
  }
  k=0;
  if (index_ref>=index_sen)
  {if (index_sen>=R)
  index1=index_sen-R;
  else index1=0;
  if (index_ref+R<=M)
  index2=index_ref+R;
  else index2=M;
  for (i=index1;i<index2;i++)

```

```

    {SLD_ref[k]=SLD_ref_in[i];
      SLD_sen[k]=SLD_sen_in[i];
      DFB[k]=DFB_in[i];
      k++;
    }
    N=k+1;
  }

  else {if (index_ref>=R)
index1=index_ref-R;
  else index1=0;
  if (index_sen+R<=M)
index2=index_sen+R;
  else index2=M;
  for (i=index1;i<index2;i++)
    {SLD_ref[k]=SLD_ref_in[i];
      SLD_sen[k]=SLD_sen_in[i];
      DFB[k]=DFB_in[i];
      k++;
    }
    N=k+1;
  }
  printf("TOTAL sample points is:N=%d\t",N);
/***** Do a five points average of dates just read in *****/

for(i=0;i<(N-4);i++)
  {SLD_sen[i]=(SLD_sen[i]+SLD_sen[i+1]+SLD_sen[i+2]+SLD_sen[i+3]
    +SLD_sen[i+4]+SLD_sen[i+5])/5;
    SLD_ref[i]=(SLD_ref[i]+SLD_ref[i+1]+SLD_ref[i+2]+SLD_ref[i+3]
    +SLD_ref[i+4]+SLD_ref[i+5])/5;
    DFB[i]=(DFB[i]+DFB[i+1]+DFB[i+2]+DFB[i+3]+DFB[i+4]+DFB[i+5])/5;
  }
  N=N-4;

/***** Normalization *****/

float DFB_sum, SLD_sen_sum, SLD_ref_sum;
  SLD_sen_sum=0.0;
  SLD_ref_sum=0.0;
  DFB_sum=0.0;
  for (i=0;i<N;i++)
    {SLD_sen_sum = SLD_sen_sum+SLD_sen[i];
      SLD_ref_sum = SLD_ref_sum+SLD_ref[i];
      DFB_sum= DFB_sum+DFB[i];
    }

```



```

    }
    for (i=0; i<N; i++)
    { SLD_sen[i]=SLD_sen[i]-(SLD_sen_sum/N);
      SLD_ref[i]=SLD_ref[i]-(SLD_ref_sum/N);
      DFB[i]=DFB[i]-(DFB_sum/N);
    }
    *****/

    int flag1=1,flag2=0;
    float sum1=0,sum2=0;
    for (i=0;i<N;i++)
    { if ((i>1)&&(DFB[i]>0)&&(DFB[i-1]<=0))
      flag2=1;
      if (i>(N-3*np)&&(DFB[i]>0)&&(DFB[i-1]<=0))
      flag1=0;
      sum1+=DFB[i]*flag1*flag2;
      sum2+=flag1*flag2;
    }
    for (i=1;i<N;i++)
    DFB[i]=DFB[i]-sum1/sum2;
    /***** find the period(cross points) of DFB[i] with x-axis *****/
    /* printf("began to process DFB side to find period etc\n"); */
    /* period_0[j] is x-position of last point of the jth period
    period_1[j] is the period length(T) of jth period
    period_1[j]=period_0[j+1]-period_0[j]
    *****/

    float period_0[Num],period_1[Num];
    int j=0,Number_period;
    int last[Num],Np[Num];
    k=1;
    for (i=0;i<N;i++)
    { if ((a[i]*a[i+1]<=0)&&(a[i-1]<a[i])&&(a[i]<a[i+1])&&(a[i+1]<a[i+2]))
      { period_0[j]=i+(a[i]/(a[i]-a[i+1]));
        last[k]=i;
        k++;
        j++;
      }
    }
    Number_period=j;
    printf("Number of periods of DFB=%d\n",Number_period);

    for (j=0; j<Number_period; j++)
    { period_1[j]=period_0[j+1]-period_0[j];

```

```

        Np[j]=last[j+1]-last[j];
    }
    printf("\n");
/***** find the coordinate x0 of each points *****/

    float x0[Max_samples],x1[Max_samples],x2[Max_samples];
    float Nc,Ncp,q;
    int Nx0;
    Nc=period_0[0];
    Ncp=period_0[1];
    Nx0=(int)Nc;
    q=(float)Nx0;
    x0[Nx0]=(q-Nc)/(Ncp-Nc);
    i=0;
    while (i<(Number_period-1))
    {Nc=period_0[i];
    Ncp=period_0[i+1];
    for (j=(int)period_0[i]+1;j<=Ncp;j++)
        x0[j]=i+(j-Nc)/(Ncp-Nc);
        i++;
        x0[j]=i+(j-Ncp)/(Ncp-Nc);
    }
/***** set new x grid values for adjusted data x1[i] *****/

    float dx;
    dx=1/(float)np;
    int Nj=np*(Number_period-1);
    for (i=0;i<=Nj;i++)
        x1[i]=(float)i*dx;
/***** calculate corrected sen and ref data *****/

    float ys[Max_samples],yr[Max_samples];
    j=0;
    for (i=Nx0;i<(N-1);)
    {d=x0[i];
    b=x0[i+1];
    y=x1[j];
    if ((d<y)&&(b>=y))
    {dxa=y-d;
    dxb=b-y;
    ys[j]=(SLD_sen[i]*dxb+SLD_sen[i+1]*dxa)/(dxa+dxb);
    yr[j]=(SLD_ref[i]*dxb+SLD_ref[i+1]*dxa)/(dxa+dxb);
    j++;
    }
}

```

```

    else i++;
/*****out put the raw data max min and diff*****/
int maxsj=0; /*max sensor x axis position*/
int maxrj=0; /*max reference x axis position*/
float maxys=ys[0]; /*max sensor y axis value*/
float maxyr=yr[0]; /*max reference y axis value*/
for (int m=1;m<j;m++)
{if (ys[m]>maxys)
    { maxys=ys[m];
    maxsj=m;
    }
if (yr[m]>maxyr){
maxyr=yr[m];
maxrj=m;
}
}
float peakdist=maxrj-maxsj;
printf(" \nraw data sensing sensor peak is:%f, at x axis %d\n", maxys, maxsj);
printf("raw data reference sensor peak is %f, at x axis %d\n", maxyr,maxrj);
printf("raw data peak fringe distance is: %f\n\n",peakdist);
/***** correlation t *****/

float corr[2*Max_samples],peak[500],pcorr_0[500];
float peak_max=0,peak_min=0, c=0;
float jmax,jmin,y1,y2,y3,dp,u,v,w;
int jm;
int Num_peak_corr;
for (i=0;i<N*2;i++)
corr[i]=0;
for (k=-(Nj-1);k<Nj;k++)
{for (i=0;i<Nj;i++)
{if((i-k)>=0&&((i-k)<Nj))
corr[k+Nj]=corr[k+Nj]+ys[i]*yr[i-k];
c=corr[k+Nj-1];
}
if (c>peak_max)
{peak_max=c;
jmax=k;
}
If (c<peak_min)
{peak_min=c;
jmin=k;
}
x2[k+Nj]=(float)k/(float)np;

```

```

    }
    printf("jmax=%f\tjmin=%f\n",jmax,jmin);
/***** write correlation data to file: corr.dat *****/

    if ((fpc=fopen("correlation.dat","w"))==NULL)
    {printf("can not write to file:correlation.dat\n");
    exit(1);
    }
    for (i=0;i<2*N-1;i++)
        fprintf(fpc,"%f\t%f\n",x2[i],corr[i]);
fclose(fpc);
peak_min=100;
peak_max=-100;
j=1;
jm=1;
for (k=jmax-ng;k<(jmax+ng);k++)
    {if (corr[k+Nj]*corr[k+Nj+1]<0)
        {if(peak_min<0)
            {y2=peak_min;
            peak_min=100;
            }
        else
            {y2=peak_max;
            peak_max=-100;
            }
        y1=corr[jm-1];
        y3=corr[jm+1];
        u=y2;
        v=0.5*(y3-y1);
        w=0.5*(y1+y3-2*y2);
        peak[j]=u-0.25*v*v/w;
        dp=-0.5*v/w;
        dp=corr[k+Nj]/(corr[k+Nj]-corr[k+Nj+1]);
        pcorr_0[j]=(k+dp)/np;
        j++;
        }
    else
        {if((corr[k+Nj]<0)&&(corr[k+Nj]<peak_min))
            {peak_min=corr[k+Nj];
            jm=k+Nj;
            }
        if ((corr[k+Nj]>0)&&(corr[k+Nj]>peak_max))
            {peak_max=corr[k+Nj];
            jm=k+Nj;
            }
        }
    }

```

```

    }
  }
}
Num_peak_corr=j;
printf("Number of peaks in correlation within jmax+/-2500 is:
%d\n\n",Num_peak_corr);

/***** use crossing to find central peak *****/

int peak_order=1;
peak_max=peak[1];
for (i=1;i<Num_peak_corr-1;i++)
{ if (peak[i]>peak_max)
  { peak_max=peak[i];
    peak_order=i;
  }
}
printf("the order of possible maximum peak is:%d ",peak_order);
printf("peak value is:%f\n\n",peak_max);
int p[7],hcp;
float pk0,pk1,pk2,pk3,pk4,pk5,pk6;
float cpn,cpn1,cpn2,cpn3,cpn4,cpn5;
float cumpk[7];
int realpeak;
float cummin=100000.0;
for (i=0;i<7;i++)
cumpk[i]=0;
p[0]=peak_order;
p[1]=p[0]-2;
p[2]=p[0]+2;
p[3]=p[0]-4;
p[4]=p[0]+4;
p[5]=p[0]-6;
p[6]=p[0]+6;
for (m=1;m<30;m++)
{ K=2*m;
  printf("check the central peak using +/-%d fringes:\n",K);
  pk0=peak[p[0]+K]-peak[p[0]-K];
  cumpk[0]+=fabs(pk0);
pk1=peak[p[1]+K]-peak[p[1]-K];
  cumpk[1]+=fabs(pk1);
pk2=peak[p[2]+K]-peak[p[2]-K];
  cumpk[2]+=fabs(pk2);
pk3=peak[p[3]+K]-peak[p[3]-K];

```

```

    cumpk[3]+=fabs(pk3);
pk4=peak[p[4]+K]-peak[p[4]-K];
    cumpk[4]+=fabs(pk4);
    pk5=peak[p[5]+K]-peak[p[5]-K];
    cumpk[5]+=fabs(pk5);
    pk6=peak[p[6]+K]-peak[p[6]-K];
    cumpk[6]+=fabs(pk6);
        printf("pk0=%f;pk1=%f;pk2=%f;pk3=%f;pk4=%f\n",pk0,pk1,pk2,pk3,pk
4);
    printf("pk5=%f;pk6=%f\n",pk5,pk6);
printf("peak[p0+%d]-peak[p0-%d]=pk0=%f\n",K,K,pk0);
    printf("peak[p1+%d]-peak[p1-%d]=pk1=%f\n",K,K,pk1);
printf("peak[p2+%d]-peak[p2-%d]=pk2=%f\n",K,K,pk2);
printf("peak[p3+%d]-peak[p3-%d]=pk3=%f\n",K,K,pk3);
    printf("peak[p4+%d]-peak[p4-%d]=pk4=%f\n",K,K,pk4);
    printf("peak[p5+%d]-peak[p5-%d]=pk5=%f\n",K,K,pk5);
    printf("peak[p6+%d]-peak[p6-%d]=pk6=%f\n",K,K,pk6);
if ((cumpk[0]<cumpk[1])&&(cumpk[0]<cumpk[2]))
    {printf("hcp=%d is central peak.\n\n",p[0]);
    hcp=p[0];}
    else if ((cumpk[1]<cumpk[3])&&(cumpk[1]<cumpk[0]))
    {printf("hcp=%d is central peak.\n\n",p[1]);
    hcp=p[1];
        }
    else if ((cumpk[2]<cumpk[4])&&(cumpk[2]<cumpk[0]))
    {printf("hcp=%d is central peak.\n\n",p[2]);
    hcp=p[2];
        }
    else {
        printf("peak not among %d,%d,%d using
        K=40\n\n",p[0],p[1],p[2]);        float mincumpk=100000;
        for (i=0; i<7;i++){    if (cumpk[i]<mincumpk){
        mincumpk=cumpk[i];
        realpeak=i;
        }
        }
        hcp=p[realpeak];        printf("hcp=%d is central peak.\n\n",p[realpeak]);
    }
}
printf("using crossing to find central peak:\n");
if (hcp>0)
{cpn=(pcorr_0[hcp]+pcorr_0[hcp-1])/2;
printf("central peak position= %f\n",cpn);
cpn1=(pcorr_0[hcp+1]+pcorr_0[hcp-2])/2;

```

```

printf("use 2 crossing to find peak postion=%f\n",cpn1);
    cpn2=(pcorr_0[hcp+2]+pcorr_0[hcp-3])/2;
printf("use 3 crossing to find peak postion=%f\n",cpn2);
cpn3=(pcorr_0[hcp+3]+pcorr_0[hcp-4])/2;
printf("use 4 crossing to find peak postion=%f\n",cpn3);
    cpn4=(pcorr_0[hcp+4]+pcorr_0[hcp-5])/2;
printf("use 5 crossing to find peak postion=%f\n",cpn4);
cpn5=(pcorr_0[hcp+5]+pcorr_0[hcp-6])/2;
printf("use 6 crossing to find peak postion=%f\n\n\n",cpn5);
    }
    else printf("Something wrong,check the data carefully\n\n\n");
for (int i=0;i<7;i++) {
        printf("The Sum of the difference assuming p[%d] is
        central is: %f\n", i,cumpk[i]);
    }
If ((fp3=fopen("result.dat","a"))==NULL)
    {printf("can not write to file:result.dat\n");
    exit(1);
    }
fprintf(fp3,"%f\n",cpn);
fclose(fp3);
return 0;
/***** resolution enhancement *****/
*****/first:find negative peak of central fringe*****/
float reso[2*F],reso_sum[2*F],cpn_f;
int lcpn,rcpn;
lcpn=rcpn=cpn;
for (i=0;i<(ceil(period_corr/2)+1);i++)
    {if (corr[lcpn-2]>corr[lcpn-1]&&corr[lcpn-1]>=corr[lcpn]&&
    corr[lcpn]<=corr[lcpn+1]&&corr[lcpn+1]<corr[lcpn+2])
        break;
        lcpn--;
    }
printf("lcpn=%d\n",lcpn);
for (i=0;i<(ceil(period_corr/2)+1);i++)
    {if (corr[rcpn-2]>corr[rcpn-1]&&corr[rcpn-1]>=corr[rcpn]&&
    corr[rcpn]<=corr[rcpn+1]&&corr[rcpn+1]<corr[rcpn+2])
        break;
        rcpn++;
    }
printf("rcpn=%d\n",rcpn);
/*****correlation with a generated cosine curve to enhance resoltuon.*****/
/* enhanced resolution=1/(sample/fringe)*(500/sample)*****/
/* if 50 samples per fringe, enhance 1/25000*****/

```

```

/*generate a cosine curve and have correlation with it*****/
for(i=0;i<2*F;i++) //F=500
reso_sum[i]=0;
for (i=0;i<2*F;i++)
{for(j=0;j<(rcpn-lcpn+1);j++)
{reso[i]=0.5*cos(2.0*pi*((float)(lcpn+j)-((float)(cpn-1)+
((float)i/(float)F)))/period_corr);
reso_sum[i]+=corr[lcpn+j]*reso[i];
}
}
For (i=2;i<2*F-2;i++)
{if (reso_sum[i-2]<reso_sum[i-1]&&reso_sum[i-1]<=reso_sum[i]&&
reso_sum[i]>=reso_sum[i+1]&&reso_sum[i+1]>reso_sum[i+2])
break;
}
printf("i for resolution enhancement=%d\n\n",i);

/*****find data after resolution,save to file:temperature.dat *****/
cpn_f=(float)cpn+(((float)i-F)/F)-(float)N;
cpn_f=(float)cpn+(((float)i-F)/F);
printf("cpn_f(final peak point of corr[i])is=:%f\n",
cpn_f-np*(Number_period-1)+1);
printf("peaks distance is(in fringes)[cpn_f-np*(Number_period-1)+1]/np)=%f\n",
(cpn_f-np*(Number_period-1)+1)/np);

/***** write to file: temperature(*fpt) *****/
if( (fpt=fopen("temperature_0508double.dat","a"))==NULL)
{printf("can not write and append to file:temperature_0508double.dat\n");
exit(1);
}
fprintf(fpt,"%-15s\t%-12s\t%f\t%f\n",filename,temp,
cpn_f-np*(Number_period-1)+1,(cpn_f-np*(Number_period-1)+1)/np);
fclose(fpt);

/*****/

return 0;
}

```


VITA

Zhaoxia Xie received a B.S. degree in physics from Shandong University in 1988. From August 1988 to August 1996, she worked at the Environmental Protection Bureau of Dezhou as an engineer and section manager in water pollution monitoring, in charge of the city's industrial water pollution monitoring and management. She started graduate studies in 1996, and in Aug. 1999 she received a M.S. degree in physics from Shandong University.

In Aug. 1999 she came to the United States as a research assistant and teaching assistant in the Physics Department, University of Houston and in December 2000 she received her M.S. in physics. She entered the graduate school of Texas A&M University in Jan. 2001 as a research assistant in the Institute of Solid State Electronics, Photonics and Nano-engineering, under Dr. Henry F. Taylor and Dr. Ohannes Eknayan. She worked as an intern at the NEC Laboratory America Incorporated from Aug. 2005 to Jan. 2006.

Her main interests include fiber optic sensors, optic components, optical fiber networks, biomedical imaging and optical-related testing.

Her permanent address is:

North Dexing Street, Dongdi, #3, Suite 104,

Dezhou, Shandong, China, 253000

Email address: zxxie@ece.tamu.edu